Dendrite-growth resistance in solid state electrolytes

Chenjie Gan†, Syuan Song†, Zikang Yu, Brian Sheldon, Pradeep Guduru and Kyung-Suk Kim*
School of Engineering, Brown University, Providence, RI 02912
† Co first author
*Corresponding author: kyung-suk_kim@brown.edu

Abstract

We address dendrite growth resistance in solid electrolytes in all-solid-state Li-ion batteries. First, we introduce a dendrite-growth model in the electrical, ionic-flow, temperature, and stress fields in the solid-state electrolyte. The model analysis shows that the applied electrode potential generates field singularities at the dendrite/crack tip, driven by electrochemical ion-deposition pressure and the thermal-conductivity jump at the dendrite/electrolyte interface. An extended J-integral is introduced to characterize the stress and temperature-gradient singularities and associated driving forces of the dendrite/crack tip in the heat-generating medium. These singularities are then used to construct universal threshold-current-density diagrams of dendrite/crack growth in solid electrolytes. From the universal diagram, the resistance to dendrite/crack growth is defined. This resistance depends on the dendrite/crack length, film thickness, and the properties of the electrochemically active solid-state electrolyte. These properties include ion conductivity, thermal conductivity, thermal expansion coefficient, elastic moduli, and toughness against dendrite/crack growth. The analyses show that the driving force from thermal stresses induced by Joule heating of the ionic current in the electrolyte is particularly significant for short dendrite/crack structures. The polarity of the temperature gradient in the electrolyte is found to be a primary factor in determining the threshold current density for short-dendrite/crack growth. The analysis offers methods for testing the dendrite/crack toughness of the electrochemically active solid-state electrolyte. It also guides the design of battery-cell packing sequences to maximize resistance to dendrite/crack formation and growth along the cooling path.

Keywords:

1. Solid-state electrolyte
2. Joule-heating-induced temperature gradient
3. Thermal stress intensity factor
4. Electro-chemo-mechanical embrittlement/toughening

5. Threshold current density
6. Dendrite/crack growth resistance

1. Introduction

Recently, we found that applying a moderate temperature gradient across a thin-film solid electrolyte (LLZTO) can triple the critical current density (CCD) of all-solid-state batteries (ASSBs) (Yu et al., 2026). Over the past decade, safe oxide- or sulfide-based ASSBs have been developed for high-energy-density applications (Mercier et al., 1981, Thangadurai et al., 2004). These batteries are non-volatile and highly resistant to catastrophic short-circuit failure caused by metal dendrite growth in their solid-state electrolytes (SSEs) (Sandoval et al., 2025, Manthiram et al., 2017, Janek and Zeier, 2016, Monroe and Newman, 2004, Monroe and Newman, 2005). Dendrite formation and growth are key factors in determining the cycle life and charging rate of ASSBs. To address this, researchers have focused on suppressing dendrite formation through lattice-structure optimization and targeted doping, thereby achieving higher charging-current densities in SSEs (Kwatek et al., 2020, Xia et al., 2016). More recently, it has been recognized that, unlike liquid electrolytes, dendrites in SSEs tend to generate internal stress fields that can lead to crack-like propagation (Porz et al., 2017, Fincher et al., 2022, Zhang et al., 2026). In this paper, we develop a theory of thermo-mechanical dendrite growth for which we refer to the crack-like dendrite growth in SSEs as "dendrite/crack (d/c) growth." While dendrite growth in liquid electrolytes is strongly influenced by operating temperature, the effect of temperature on d/c growth in SSEs is often considered minimal. However, we demonstrate that d/c growth in SSEs is sensitive to Joule heating of the ion current, the cooling path, and thus to temperature gradients, thermal conductivity, and thermal expansion in the electrolyte. Therefore, controlling temperature-gradient in the SSE is crucial for designing all-solid-state batteries that resist dendrite growth.

To model d/c growth in an SSE, we first analyze four static fields: electrostatic, ion flow, temperature, and stress. These fields surround a stationary d/c extruded into an SSE from a negative electrode (NE) of an ASSB during charging. This analysis shows how the NE-dendrite/SSE interface distinguishes between stagnant and active Li deposition zones. It also reveals how the stagnant zone creates static fields focused on the d/c tip. These fields affect the criticality of d/c advancement. We identify the threshold current density (TCD) for d/c growth in solid electrolytes. TCD is the minimum far-field ion current density needed for a single d/c to grow in a thin-film SSE. By contrast, the commonly referenced CCD is the average ion current density

that causes battery failure after the formation of complex dendrites. This failure can occur after multiple charge/discharge cycles (Lu et al., 2021). Our study focuses on lithium ions (Li^+) as the charge carriers, with the dendrite as solid lithium metal. However, the formalism applies to other mobile metallic ions. The ion current in the SSE produces Joule heating. This phenomenon is similar to those well-studied in liquid and polymer electrolytes (Yuan et al., 2024, Tran et al., 2022).

The ion current also facilitates lithium deposition at the dendrite/electrolyte interface, causing the lithium dendrite to expand its volume within the confined opening of the SSE crack faces (Porz et al., 2017). The deposition process continues until the electric potential balances the pressure on the crack faces, the distribution of which is governed by the Butler-Volmer equation (Butler, 1924, Erdey-Grúz and Volmer, 1930). In this paper, the pressure distribution is assumed solely regulated by the elastic deformation of the SSE to balance the Butler-Volmer pressure. A long d/c develops an interface pressure below the dendrite metal's yield stress. For an intermediate length d/c, the interface pressure and its gradient may induce plastic flow, and we will treat it elsewhere in a sequel paper. As a result, the pressure distribution on the SSE crack face creates a heightened triaxial tensile stress field near the d/c tip. This intensified stress field can be measured by a crack-face-pressure(cfp)-induced stress intensity factor $K_I^{(cfp)}$. Additionally, the $K_I^{(cfp)}$ field encourages electronic lithium deposition and/or micro-cracking at near-tip grain-boundaries, leading to electrochemical embrittlement and/or micro-crack toughening (Pustorino et al., 2024, Zhang et al., 2025). Recently, detailed athermal analyses of dendrite growth related to the $K_I^{(cfp)}$ field in LLZO have been discussed in literatures (Fincher et al., 2022, Porz et al., 2017, Mukherjee et al., 2023).

This paper shows that ion-current Joule heating creates a significant temperature-gradient concentration near the d/c tip. This gradient coupled with thermal expansion leads to an additional stress focusing, beyond the $K_I^{(cfp)}$ stress field observed near the d/c tip, when the SSE is cooled from either electrode side. This additional concentration occurs when the thermal conductivity ratio of lithium metal to SSE is much greater than one. The typical range is 10 to 200 for lithium's 85 W/(m·K) thermal conductivity (Ho et al., 1972). The temperature gradient from heat flowing into or out of the dendrite generates a singular crack-opening or -closing thermal stress field. This field is characterized by the Joule-heating-induced thermal stress intensity factor $K_I^{(ts)}$. Notably, this parameter $K_I^{(ts)}$is much larger than the parameter $K_I^{(cfp)}$ for short d/c's exposed to high ion-

current density. The Seebeck effect and the expansion of the SSE from temperature-dependent lithium-ion concentration may also influence the stress intensity field at the d/c tip (Sharafi et al., 2016). However, these additional factors are considered negligible compared to the contributions from the $K_I^{(ts)}$ and $K_I^{(cfp)}$ fields. The external stress intensity factor $K_I^{(ext)}$ field from boundary tractions and body forces adds to the total stress intensity factor and affects dendrite growth. Concerning the near-tip field in an SSE and the d/c growth, the singular stress-intensity field has been directly observed using photoelasticity (Athanasiou et al., 2024, Fincher et al., 2026). Our recent experiments reported elsewhere (Yu et al., 2026) show that an external temperature gradient caused by positive-electrode (PE) cooling and NE heating can increase the CCD of a coin-cell battery by about three times. Previous studies have explored how temperature affects material properties (Sharafi et al., 2016, Hess, 2018). However, the thermal stresses affecting dendrite propagation under temperature gradients in SSEs are addressed here for the first time.

Regarding the $K_I^{(cfp)}$, $K_I^{(ts)}$, and $K_I^{(ext)}$ fields, while the conventional J-integral (Rice, 1968) and the Irwin relation (Irwin, 1957) serve to evaluate the stress-intensity fields, the analysis of mechanical, thermal, and electrochemical multi-physics fields necessitates an extended J-integral. This paper introduces an extended J-integral specifically for d/c growth in SSE, that includes entropy and temperature distributions. The extended J-integral evaluates the parameters $K_I^{(cfp)}$ and $K_I^{(ts)}$ for two primary boundary conditions – a free traction and a partially fixed displacement - in simulating the lithium-ion current field within a thin-film SSE cooled from NE or PE. The ion current and associated heat generation create a stress field in the SSE and contribute to the d/c-tip energy release rate through the $K_I^{(cfp)}$ and $K_I^{(ts)}$fields. For a small nominal d/c-tip process-zone size $r_0 \ll a$, we introduce a small-scale process-zone d/c growth criterion – a d/c begins to grow when the combined value, under a threshold (ion)-current density, $i^{(tcd)}$, reaches the d/c-growth toughness.

In this paper, we refer to $K_I^{(ts)}$ for $K_I^{(total)} - K_I^{(cfp)} - K_I^{(ext)}$. Here, $K_I^{(ts)}$ is defined as a nominal stress intensity factor that asymptotically approaches $\sqrt{E^* J^{(ts)}}$ near a d/c tip. Here, E^* is the plane-strain Young's modulus and $J^{(ts)}$ the extended J-integral of the thermal stress field for a d/c tip with a small-scale process zone. In this zone, chemical Li deposition processes at the growing dendrite tip and nearby grain boundaries reduce the SSE's dendrite-growth toughness (Pustorino

et al., 2024). Some eigenstrain-producing mechanisms increase the toughness (Zhang et al., 2025). These phenomena illustrate two concepts: electrochemical embrittlement and micro-mechanical toughening. More recently, in a system of garnet-type solid electrolyte, toughness was measured to be decreased with the increasing current (Fincher et al., 2026). The parameter ξ, hereafter referred to as the embrittlement/toughening factor (ET factor), quantifies the extent of these embrittlement and toughening effects, which are typically managed by doping with various chemical elements (Zhang et al., 2024) and controlling the grain and grain-boundary mechanical properties (Xie et al., 2024, Jia et al., 2024). Diverse dopants are used to stabilize the crystal structures of SSEs (Zhou et al., 2022, Xia et al., 2016). They can also modify their bulk properties, such as ionic conductivity, thermal conductivity, thermal expansion coefficient, and elastic moduli, or adjust the characteristics of the SSE/dendrite interface (Zhang et al., 2024, Sharafi et al., 2017b). However, the ET factor ξ for d/c growth toughness $K_{IC}^{(dcg)} = \xi K_{IC}$ of electro-chemo-mechanically active d/c tips in an SSE has not been well defined or measured. In this paper, we rigorously define the ET factor and provide a measurement method for it. Then, the ET factor is used to address dendrite growth resistance (DGR) by investigating the TCD for d/c growth. All analyses are presented on a non-dimensionalized, universal TCD (U-TCD) diagram, which displays a single, collapsed curve for various SSEs. The U-TCD diagram is expected to aid in strategic decisions regarding SSE material selection, manufacturing methods, dopant selection, structural design, external mechanical loading, and thermal management.

2. Analysis of fundamental multi-physics continuum fields in SSE

In this section, we analyze the stress, temperature and electrical fields, as well as the steady heat and ion flows driven by associated potentials applied to a stationary d/c in SSE, up to the onset of growth. From our analysis, we introduce an extended J-integral with multi-physical Helmholtz free energy potential to extract key parameters that establish a criterion for d/c growth. These parameters are influenced by the far-field ion-current density, the material properties of the SSE, the specimen's geometry, and the boundary conditions. To establish a universal relationship for d/c growth criticality, we analyze the driving force of i^{∞} with the extended J-integral for a set of the SSE material properties, a primary specimen geometry, and boundary conditions, as shown in Fig. 1(a). The primary SSE specimen geometry is a thin film geometry of thickness W and height H for $H/W \gg 1$. Details of the boundary conditions are presented in Section 2.4. Figure 1(b) shows an optical image of a d/c extended from an NE tip in an LLZTO SSE. Figures 1(c) exhibits photo-elastic fringes around a d/c tip, revealing stress-singularity field near the d/c tip (Athanasiou et al., 2024). Here, we use the stress intensity factor of the singular field as a fracture-toughness parameter to calibrate the d/c growth resistance. The toughness is typically governed by d/c-tip embrittlement caused by isolated grain-boundary dendrite formation (Pustorino et al., 2024) and toughening via micro-crack formation (Zhang et al., 2025), respectively. The two representative d/c-tip embrittlement and toughening processes are considered to result in the electro-chemo-mechanical ET factor ξ. To establish a universal relationship between TCD and the ET factor, all governing equations are normalized, using Greek subscript indices, with Einstein's summation convention, to represent the two-dimensional components 1 and 2.

2.1 Equations of thermomechanical stress and deformation fields:

Mechanical equilibrium of the stress field in SSE is represented in a normalized form as

$$\frac{\partial \bar{\sigma}_{\beta\alpha}}{\partial \bar{x}_{\beta}} + \bar{b}_{\alpha} = 0 \tag{1}$$

where $\bar{\sigma}_{\beta\alpha} = \sigma_{\beta\alpha}/\mu$ with stress components $\sigma_{\beta\alpha}$ and the SSE shear modulus μ; $\bar{x}_\beta = x_\beta/W$ with spatial coordinates x_β and the SSE film thickness W; $\bar{b}_\alpha = b_\alpha W/\mu$ with body-force components b_α. Then, the thermoelastic constitutive relation of the SSE is normalized as

$$\bar{\sigma}_{\beta\alpha} = \left\{\frac{\delta_{\beta\xi}\delta_{\alpha\eta}}{(1-2\nu)} + \delta_{\alpha\xi}\delta_{\beta\eta}\right\}\left\{\frac{\partial \bar{u}_\xi}{\partial \bar{x}_\eta} - \bar{\theta}\delta_{\xi\eta}\right\} \tag{2}$$

where $\delta_{\beta\xi}$ is the Kronecker delta, ν the Poisson ration of the SSE; $\bar{u}_\xi = u_\xi/W$ with local displacement components u_ξ; $\bar{\theta} = \alpha(\theta - \theta_0)$ with thermal expansion coefficient α of the SSE, local temperature θ in the SSE, and a reference temperature θ_0.

2.2 Equations of ion-current flow:

The electric field drives steady-state electrical current flow in the primary SSE specimen geometry. This electric current field is determined by Ohm's law. In this context, current consists of electron and/or ion currents. However, in an SSE, the leaking electron current density is usually negligible compared to the ion current density. As a result, the current primarily depends on the ion conductivity for a given electric potential gradient. Therefore, the steady-state ion-current density is described by

$$\bar{\imath}_\beta + \frac{\partial \bar{\Phi}}{\partial \bar{x}_\beta} = 0 \tag{3}$$

where $\bar{\imath}_\beta = i_\beta/i_{ref}$ with local ion-current density vector i_β and a reference ion-current density $i_{ref} = \sqrt{\kappa^{ion}\kappa^{th}/\alpha W^2}$ for which κ^{ion} and κ^{th} are the ion and thermal conductivities of the SSE, respectively; $\bar{\Phi} = \phi\kappa^{ion}/i_{ref}W$, for electric potential ϕ. Additionally, charge conservation is required for the ion-current field, expressed as

$$\frac{\partial \bar{\imath}_\beta}{\partial \bar{x}_\beta} = 0 \tag{4}$$

2.3. Equations of heat flow:

A steady-state heat flow field in SSE is governed by the Fourier law of heat conduction for the heat flux q_β caused by Joule heating of i_β as

$$\frac{\partial \bar{\theta}}{\partial \bar{x}_\beta} + \bar{q}_\beta = 0 \tag{5}$$

for which $\bar{q}_\beta = \alpha q_\beta W/\kappa^{th}$. Then, the requirement of energy conservation on q_β for the heat generation of i_β 's Joule heating is expressed as

$$\frac{\partial \bar{q}_\beta}{\partial \bar{x}_\beta} - \bar{\imath}_\beta \bar{\imath}_\beta = 0 \tag{6}$$

2.4. Boundary conditions:

Referring to Fig. 1(a), we consider four primary boundary conditions for a thin-film SSE with a single-edge d/c: (1) a straight film with (NEc & PEi), (2) a bent film free of traction with (NEc & PEi), (3) a straight film with (PEc & NEi), and (4) a bent film free of traction with (PEc & NEi). Here, (NEc & PEi) stands for NE cooling with PE-side insulation, and (PEc & NEi) for PE cooling with NE-side insulation. For the straight film, the normal displacement of the insulating face is held fixed to maintain flatness. In contrast, a traction-free film warps due to bending caused by temperature gradients in the SSE resulting from body Joule heating and boundary cooling. No in-plane tensile/compression forces or bending moments are applied to the film's cross-section far from the d/c plane. The dendrite/SSE interface boundaries have a normal traction distribution

$$\sigma_n(x_1) = -\frac{zFi^\infty\left(x_1 + R^{int}\kappa^{ion}\right)}{V_m\kappa^{ion}}, 0 \le x_1 \le a << W \tag{7}$$

where z is the number of electrons involved in the unit electrode reaction, F the Faraday constant, R^{int} the interface resistance, and V_m the molar volume of the ion. Equation (7) comes from the condition of no deposition current on the dendrite surface when there is a steady ion current in SSE for a stationary d/c. This result uses the linearized Butler-Volmer equation (Butler, 1924, Erdey-Grúz and Volmer, 1930) for low effective over-potential. Here, the traction is balanced by the electric potential distribution in the SSE as

$$\phi = \frac{i^\infty\left(x_1 + R^{int}\kappa^{ion}\right)}{\kappa^{ion}} \tag{8}$$

With this over-potential jump along the dendrite/SSE interface, the potential on the Li dendrite surface along the interface remains constant, the same as the NE potential. Turning to thermal

effects, for the four primary boundary conditions, the thermal boundary conditions specify that the temperatures at the SSE/NE and SSE/dendrite interfaces remain equal and constant for $\kappa_{(Li)}^{th}/\kappa_{(SSE)}^{th} \gg 1$. Other than the SSE/dendrite boundary conditions, the temperature at the cooling face of the SSE is kept constant, while an adiabatic boundary condition is applied at the insulating face. Furthermore, analytical solutions of the bending curvature, and the stress, and temperature distributions on the film's cross-section far away from the d/c plane for the four primary boundary conditions are presented in the Appendix. In contrast, details of the stress and temperature distributions near the d/c tip for the four primary cases are obtained using finite element method (FEM) analysis and are presented in the following section.

2.5 FEM analysis of multiple stress-intensity fields of a dendrite/crack

The coupled electro-thermo-mechanical partial differential equations (PDEs) governing the system are solved using the FEM in COMSOL Multiphysics 5.2 (COMSOL-Inc.). Specifically, the governing equations—force balance (solid mechanics), Fourier heat conduction (heat transfer in solids), and Poisson's equation (electrostatic field)—are implemented through the Solid Mechanics, Heat Transfer in Solids, and Coefficient Form PDE modules, respectively. To capture the physical configuration, the computational domain in Fig. 1(a) models the upper half of the SSE as a plane strain problem, having dimensions of 1 mm thickness (W) and 6.35 mm (half) height (H). Within this domain, a lithium metal dendrite of variable length, denoted as *a,* is positioned along the symmetric axis, initiating from the NE side of the electrolyte. In this study, we employed LLZO as the solid for the SSE FEM model. The corresponding material properties—including Young's modulus, Poisson's ratio, thermal expansion coefficient, thermal conductivity, and ionic conductivity—are provided in Table 1. Boundary conditions were implemented as outlined in Section 2.4. To ensure accuracy, the convergence test for the FEM using an extended J-integral, defined in the next section, was performed with a mesh comprising approximately 100,000 quadrilateral elements, which consisted of 570,000 nodes with non-uniform sizing. Notably, near the d/c tip, refinement allows for a minimum element size of 0.1 μm, enabling effective resolution of stress singularities and temperature gradients.

Figure 2(a) illustrates the FEM analysis results of the near-tip stress distributions, labeled $\sigma_{yy}^{(ts)}$, $\sigma_{yy}^{(cfp)}$, and $\sigma_{yy}^{(total)}$, for $a = 1,10,100\ \mu m$, respectively, at the critical stress intensity ξK_{IC} (=

$K_I^{(cfp)} + K_I^{(ts)}$) of 0.95 $MPa\sqrt{m}$ with $\xi = 0.58$, for NE cooling of a straight SSE film. The K_{IC} of 1.64 $MPa\sqrt{m}$ is a reported value based on nano-indentation fracture tests of an LLZO (Wolfenstine et al., 2013). The ξ value of 0.58 is a theoretical DFT estimation of potassium fluoride (KF)-doped LLZTO (Zhang et al., 2024). The ξ value for undoped LLZO would have been 0.12 (Sharafi et al., 2017b, Mukherjee et al., 2023). The results of $a = 1,10,100\mu m$ correspond to $\chi_{ts}\left(\equiv K_I^{(ts)}/K_I^{(cfp)}\right) = (7.032,0.152,0.001)$,TCD$= (119.1,26.6,1.0)\ mAcm^{-2}$, $K^{(ts)} = (0.83,0.13,0.001)\ MPa\sqrt{m}$, $K^{(cfp)} = (0.12,0.82,0.948)\ MPa\sqrt{m}$, respectively. The findings indicate that the crack-tip opening displacement driven by thermal stress is significantly larger than that caused by cfp in the high χ_{ts} case. Conversely, this trend is reversed in the low χ_{ts} case.

Figure 2(b) explicitly displays the stress distributions $\sigma_{yy}^{(ts)}$, $\sigma_{yy}^{(cfp)}$, and $\sigma_{yy}^{(total)}$ along the crack line for the three values of χ_{ts}, for NE cooling of a straight SSE film. It shows $1/\sqrt{r}$ stress singularities ahead of the d/c tips, where r is a distance from the d/c tip. For the short d/c of $a = 1\mu m$, the cfp distribution increases linearly with x_1, as expected. It remains relatively low, with its maximum 78.9 MPa at the d/c tip. This low maximum occurs because much of the stress intensity at the d/c tip is supported by the temperature gradient ahead of it. If the SSE had not been doped with KF, the maximum pressure would have reached a hypothetical value of 16.3 MPa. For the intermediate-length d/c of $a = 10\mu m$, the maximum pressure is $230MPa$, while the undoped SSE would have a maximum pressure of 47.6 MPa. In the case of the long d/c of $a = 100\mu m$, the maximum pressure is 80 MPa, and an undoped SSE would show a maximum pressure of 16.6 MPa. These results seem to resolve a controversy regarding the previous athermal analysis (Mukherjee et al., 2023). That analysis suggested that the maximum cfp would reach 1 GPa for a short d/c.

Figure 2(c) shows inverse-parabolic temperature distributions along the crack lines ahead of the d/c tips, exhibiting $1/\sqrt{x_1 - a}$ temperature-gradient singularities, for NE cooling of a straight SSE film. Joule heating raises the maximum temperatures in SSEs by 86, 4.3, and 0.01 K for the short, intermediate-length, and long d/c configurations, respectively. The singular temperature-gradient distribution produces an asymptotic singular stress distribution ahead of the d/c tip, as shown in Fig. 2(b). If the d/c were not there, there would be a nominal temperature gradient at $x_1 = a$. The

nominal temperature gradient and the thermally induced boundary tractions determine the thermal stress intensity factor $K_I^{(ts)}$.

Figure 2(d) exhibits FEM analysis results of the near-tip stress distributions $\sigma_{yy}^{(cfp)}$ and $\sigma_{yy}^{(total)}$ for $a = 1{,}10{,}100\ \mu m$ at the critical stress intensity of 0.95 $MPa\sqrt{m}$, like those of Fig. 2(a), but for NE cooling of a film free of traction. The results of $a = 1{,}10{,}100\mu m$ correspond to $\chi_{ts} = (1.679{,}0.048{,}0.0001)$, TCD $= (202.7{,}30.4{,}0.9)\ mAcm^{-2}$, $K^{(ts)} = (0.6{,}0.06{,}0.001)\ MPa\sqrt{m}$, $K^{(cfp)} = (0.35{,}0.89{,}0.948)\ MPa\sqrt{m}$, correspondingly.

Figure 2(e) displays the stress distributions along the crack line like those of Fig. 2(b), but for the three values of χ_{ts} of Fig. 2(d) for NE cooling of a film free of traction. For $a = 1{,}10, and 100\mu m$, the maximum cfp's were $291.2, 233.9$ and $74.4\ MPa$ at the d/c tip, correspondingly. Similarly, the maximum pressure would have reached the values of $60.2, 48.4$ and $15.4\ MPa$ for the undoped SSE.

Figure 2(f) shows inverse-parabolic temperature distributions, similar to those in Fig. 2(c), but with NE cooling of a film free of traction on both its faces. Joule heating raises the maximum temperatures in SSEs by 249.7, 5.6, and 0.01 K for the three lengths of a, respectively. The nominal temperature gradient at the d/c tip determines the thermal stress intensity factor $K_I^{(ts)}$ for the film free of traction.

Figure 3(a) presents the FEM analysis results of the near-tip stress distributions $\sigma_{yy}^{(cfp)}$ and $\sigma_{yy}^{(total)}$, similar to those in Fig. 2(a), but for PE cooling of a straight film. The results of $a = (8{,}10{,}100)\mu m$ correspond to $\chi_{ts} = (-0.246, -0.138, -0.0007)$, TCD $= (61.1{,}35.3{,}1.5)\ mAcm^{-2}$, $K^{(ts)} = (-0.31, -0.15, -0.0007)\ MPa\sqrt{m}$, $K^{(cfp)} = (1.26{,}1.09{,}0.95)\ MPa\sqrt{m}$, correspondingly. For the PE cooling, the thermal stress gradient tends to close the d/c tip, indicated by the negative sign of $K^{(ts)}$, in contrast to the opening stress field caused by the cfp can be driven by a $K^{(total)}$ field of i^{∞} is very close to but shorter than 8 μm for PE cooling. If the length is shorter than 8 μm, the required current density becomes so high that other mechanisms of dendrite growth would limit i^{∞}.

Figure 3(b) displays the stress distributions, $\sigma_{yy}^{(cfp)}$ and $\sigma_{yy}^{(total)}$, along the crack line for the three values of χ_{ts} for PE cooling of a straight film, showing negative thermal-stress singularities ahead of the d/c tips. For the three lengths of $a = (8, 10, 100)\ \mu m$, the crack-face pressure distribution for PE cooling reaches its maximum $367.1, 284.3$ and $78.4\ MPa$ at the d/c tip, respectively. As the nominal temperature gradient for PE cooling tends to close the d/c tip, more cfp is required than that of NE cooling to achieve the total stress intensity factor at the critical value.

Figure 3(c) shows near-tip inverse-parabolic temperature distributions along the crack lines ahead of the d/c tips, for PE cooling of a straight film. These distributions exhibit negative $1/\sqrt{x_1 - a}$ temperature-gradient singularities. Joule heating raises the maximum temperatures in the SSE films by 22.7, 7.6, and 0.013 K for the short, intermediate-length, and long d/c configurations, respectively.

Figure 3(d) exhibits FEM analysis results of the near-tip stress distributions $\sigma_{yy}^{(cfp)}$ and $\sigma_{yy}^{(total)}$ for $a = 8{,}10{,}100\ \mu m$ at the critical stress intensity of 0.95 $MPa\sqrt{m}$, like those of Fig. 2(a), but for PE cooling of a film free of traction. The results of $a = 8{,}10{,}100 \mu m$ correspond to $\chi_{ts} = (-0.095, -0.05, -0.0001)$, TCD $= (50.5, 34.5, 1.0)\ mAcm^{-2}$, $K^{(ts)} = (-0.10, -0.05, -0.0001)\ MPa\sqrt{m}$, $K^{(cfp)} = (1.05, 1.00, 0.95)\ MPa\sqrt{m}$, correspondingly.

Figure 3(e) displays the stress distributions along the crack line like those of Fig. 3(b), but for the three values of R_{ts} of Fig. 3(d) for PE cooling of a film free of traction. For $a = 8, 10$ and $100\ \mu m$ the maximum cfp's were $303.9, 258.9$ and $78.4 MPa$ at the d/c tip, correspondingly. Similarly, the maximum pressure would have reached the values of $62.9, 53.6$ and $16.2\ MPa$ for the undoped LLZO.

Figure 3(f) shows near-tip inverse-parabolic temperature distributions, similar to those in Fig. 3(c), but with PE cooling of a film free of traction on both its faces. Joule heating raises the maximum temperatures in SSEs by 15.5, 7.23 and 0.013 K for the three lengths of a, respectively.

3. Extended J-integral to extract the stress-intensity field of a dendrite/crack

As aforementioned, we consider the onset of the d/c extension in SSE to be determined by the critical stress intensity factor of the d/c,

$$K_I^{(cfp)} + K_I^{(ts)} + K_I^{(ext)} = K_{IC}^{(dcg)} = \xi K_{IC} \tag{9}$$

This criterion is based on the postulate that the stress-intensity fields are superposable and the d/c-tip energy release rate $\mathcal{G}_{tip}$ is related to the total d/c-tip nominal stress intensity factor K_I for a small-scale process zone size through the Irwin relation (Irwin, 1957),

$$\mathcal{G}_{tip} = \frac{1-\nu^2}{E} K_I^2 \tag{10}$$

Therefore, the stress intensity factor K_I can be obtained by evaluating $\mathcal{G}_{tip}$ with potential energy variation of the SSE for a virtual d/c growth. For the potential energy variation, the thermomechanical potential of the SSE is expressed as

$$\Pi(\boldsymbol{\varepsilon}, \theta) = \int_A (f + \hat{s}\theta) dA - \int_\Gamma \hat{\mathbf{t}} \cdot \boldsymbol{u}\, dl \tag{11}$$

for which $\boldsymbol{\varepsilon}$ represents strain tensor, f Helmholtz free energy density, $s$entropy density, and $\boldsymbol{t}$ traction. The hat symbol on $\hat{\mathrm{s}}$ and $\hat{\mathbf{t}}$ implies dead variable for variations of the potential. The Helmholtz free energy of the SSE is formulated as

$$f\left(\varepsilon_{ij}, \theta\right) = \psi - \frac{C_V}{2\theta_0}(\theta - \theta_0)^2 - s_0\theta \tag{12}$$

where C_V is the volumetric heat capacity, and ψ is the strain-energy density represented as

$$\psi = \frac{1}{2}\lambda\varepsilon_{kk}^2 + \mu\varepsilon_{ij}\varepsilon_{ij} - B\alpha(\theta - \theta_0)\varepsilon_{kk} \tag{13}$$

with λ and μ the Lame´ constants, B the bulk modulus, and ε_{ij} the strain. Here, the italic subscripts indicate 3D indices for which the summation convention is applied for repeated indices. The stress and the entropy are explicitly expressed as

$$\sigma_{ij} = \left.\frac{\partial f}{\partial \varepsilon_{ij}}\right|_\theta = \lambda\varepsilon_{kk}\delta_{ij} + 2\mu\varepsilon_{ij} - B\alpha(\theta - \theta_0)\delta_{ij} \tag{14a}$$

$$s = -\left.\frac{\partial f}{\partial \theta}\right|_{\varepsilon_{ij}} = B\alpha\varepsilon_{kk} + \frac{C_V}{\theta_0}(\theta - \theta_0) + s_0 \tag{14b}$$

Then, the energy release rate at the d/c tip is represented as

$$\mathcal{G}_{tip} \equiv \left.\frac{\partial \Pi}{\partial x_1}\right|_{(A_{in}\to 0)} = \lim_{A_{in}\to 0} \int_{\Gamma_{in}} \left((f + \hat{s}\theta) n_1 - \hat{\boldsymbol{t}} \cdot \frac{\partial \boldsymbol{u}}{\partial x_1} \right) dl \tag{15a}$$

$$= \int_{\Gamma_{cf}+\Gamma_{out}} \left(\psi n_1 - \boldsymbol{t} \cdot \frac{\partial \boldsymbol{u}}{\partial x_1} \right) dl - \int_{A_{out}} \left(b_i \frac{\partial u_i}{\partial x_1} - B\alpha\varepsilon_{kk} \frac{\partial \theta}{\partial x_1} \right) dA \tag{15b}$$

for which the contours Γ_{in} and Γ_{out} are illustrated in Fig. 4(a), A_{in} and A_{out} are areas enclosed by Γ_{in} and Γ_{out}, and Γ_{cf} is the crack-face contours. Equation (15b) is an extended J-integral expression (Rice, 1968, Wilson and Yu, 1979, Banks-Sills and Dolev, 2004). The body force b_i in the second integral of Eq. (15b) is negligible for the primary boundary value problems considered here. When a far-field temperature gradient is applied, as illustrated in Fig. 4(a), the resulting thermal stress at the d/c tip produces $1/\sqrt{r}$ stress and temperature-gradient singularities. These singularities affect both integral terms in Eq. (15b). However, the extended J-integral, which includes the area integral, remains path-independent. Figure 4(b) demonstrates that the thermomechanical field of the FEM analysis indeed exhibits the path independence. It also shows that the separate path integral of the conventional J-integral, the first term in Eq. (15b), is not path-independent. However, the conventional J-integral value approaches $\mathcal{G}_{tip}$ when Γ_{out} approaches Γ_{in} for $A_{in} \to 0$. Therefore, the near-tip nominal stress intensity factor can be obtained through the Irwin relation of Eq. (10) with $\mathcal{G}_{tip}$ as the extended J-integral expressed in Eq. (15b). For a finite size of A_{in} of the d/c tip process zone, the $\mathcal{G}_{tip}$ can be closely approximated by

$$\mathcal{G}_{tip} \approx \int_{\Gamma_{in}} \left(\psi n_1 - \boldsymbol{t} \cdot \frac{\partial \boldsymbol{u}}{\partial x_1} \right) dl + \int_{A_{in}} (s - s_0) \frac{\partial \theta}{\partial x_1}\, dA \tag{15c}$$

4. TCD criterion for SSE dendrite/crack growth and the universal TCD diagram

In the previous section, we established the necessary condition, as given by Eq. (9), for a d/c to grow when the stress intensity factor at the d/c tip reaches its critical value. In Eq. (9), $K_I^{(cfp)}$ is generated by the crack-face pressure $-\sigma_n(x_1)$ as expressed in Eq. (7). It can be expressed without loss of generality as

$$K_I^{(cfp)} = \left\{\beta\left(\frac{a}{W}\right) + \bar{\beta}\left(\frac{a}{W}\right)\frac{R^{int}\kappa^{ion}}{a}\right\}\frac{zFi^{\infty}a}{V_m k^{ion}}\sqrt{\pi a} \tag{16}$$

where $\beta(a/W)$ and $\overline{\beta}(a/W)$ respectively are crack-face-pressure and interface-resistance shape factors of the d/c length a in the SSE film of thickness W. Regarding $K_I^{(ts)}$, the temperature in the SSE is proportional to the Joule heating as expressed in Eq. (5) and the Joule heating is proportional to $(i^{\infty})^2$ as given in Eq. (6). Therefore, the thermal stress proportional to the temperature leads to the expression,

$$K_I^{(ts)} = \gamma_{\pm}\left(\frac{a}{W}\right)\sqrt{\pi a}\frac{\alpha E^*(i^{\infty})^2 W^2}{k^{th}k^{ion}} \tag{17}$$

where $\gamma_{\pm}(a/W)$ are thermal-stress shape factors of the d/c length a in the SSE film of thickness W, and $E^* = E/(1-\nu^2)$ for Youngs modulus E and the Poisson ratio ν. The $\pm$ signs imply NE and PE cooling configurations, respectively. Fig. 5(a) displays the crack-face-pressure shape factor $\beta(a/W)$ and the thermal-stress shape factors $\gamma_{\pm}^{fixed}(a/W)$ for a straight SSE film and $\gamma_{\pm}^{free}(a/W)$ for a traction-free SSE film. The shape factors were obtained through FEM simulations for various a/W values. Fore a PE cooling configuration, $\gamma_{-}(a/W)$ has a negative value. The function $\beta(a/W)$ is a slowly and monotonically increasing function with$\beta(a/W) \rightarrow 1.53$ for $a/W \rightarrow 0$. The functions $\gamma_{\pm}^{fixed}(a/W)$ and $\gamma_{\pm}^{free}(a/W)$ are slowly and monotonically decreasing function from the values at $a/W \rightarrow 0$, with $\left[\gamma_{\pm}^{fixed}(0), \gamma_{\pm}^{free}(0)\right] \rightarrow [0.463, 0.239, 0.114, 0.115]$.

Next, the onset condition of d/c growth, Eq.(9), inserting (16) and (17) into (9), determines the threshold current density for the primary boundary value problem with $K_I^{(ext)} = 0$;

$$i_{TCD}^{\infty\pm} = \Lambda_1 i_0\left\{\mp 1 \pm \sqrt{1 \pm \Lambda_2\frac{(Zi_0)^2\xi K_{IC}}{a\sqrt{a}}}\right\} \tag{18}$$

where the upper and lower signs indicate NE and PE cooling, respectively, for both straight and traction-free SSE films. In Eq. (18), an SSE material parameter i_0 has a dimension of charge-current density, d/c geometric parameters Λ_1 and Λ_2 are dimensionless functions of a/W, and another SSE material parameter Z has a unit m$A/(cm\sqrt{MPa})$. They are expressed as

$$i_0 = \frac{zF\kappa^{th}}{WV_m\alpha E^*} \tag{18a}$$

$$(\Lambda_1, \Lambda_2) = \left(\frac{\left(\beta + \bar{\beta}\frac{R^{int}\kappa^{ion}}{a}\right)a}{2|\gamma_\pm|W}, \frac{4|\gamma_\pm|W}{\sqrt{\pi}\left(\beta + \bar{\beta}\frac{R^{int}\kappa^{ion}}{a}\right)^2 a} \right) \tag{18b}$$

$$Z = \sqrt{\frac{\kappa^{th}\kappa^{ion}}{\alpha E^*}} \tag{18c}$$

Then, plotting $K_I^{(cfp)}/K_{IC}$ against the normalized far-field ion-current density, i^∞/i_{ch}, from Eq. (16), as

$$\frac{K_I^{(cfp)}}{K_{IC}} = \eta_{ch}^{(cfp)\pm}\left(\frac{i^\infty}{i_{ch}^\pm}\right) \tag{19}$$

we can construct a universal threshold current density (U-TCD) diagram, Fig. 5(b) for NE cooling and Fig. 5(b) for PE cooling. Here, we scaled i_{ref} in Eq.(3) to the characteristic current density $i_{ch}^\pm$, to have the most reduced form of the U-TCD relationship, as

$$i_{ch}^\pm = i_{ref}\sqrt{\frac{K_{IC}}{|\gamma_\pm|E^*\sqrt{\pi a}}} = \frac{Z}{W}\sqrt{\frac{K_{IC}}{|\gamma_\pm|\sqrt{\pi a}}} \tag{20}$$

On the U-TCD diagram, Eq. (19) represents a series of straight lines with slopes $\eta_{ch}^{(cfp)\pm}$ defined for various d/c lengths as

$$\eta_{ch}^{(cfp)\pm} = \frac{\beta zFaZ}{WV_m\kappa^{ion}}\sqrt{\frac{\sqrt{\pi a}}{|\gamma_\pm|K_{IC}}} \tag{21}$$

Thereafter, as we plot $K_I^{(cfp)}/K_{IC} = \xi - K_I^{(ts)}/K_{IC}$ of Eq. (9) against $i^\infty/i_{ch}^\pm$, on the U-TCD diagram, we have a bounding limit on $K_I^{(cfp)}/K_{IC}$ where Eq. (19) is also satisfied. Then, from Eq. (17), we have a parabolic relation,

$$\frac{K_I^{(cfp)}\big|_{TCD}}{K_{IC}} = \xi \mp \left(\frac{i^{\infty}}{i_{ch}^{\pm}}\right)^2 \tag{22}$$

which is plotted as a black dashed line in Fig. 5(b) for NE cooling and Fig. 5(c) for PE cooling. The $\mp$ signs represent NE and PE cooling configurations, respectively. Additionally, the limit curve, Eq. (22) for PE cooling in Fig. 5(c) splits to a dashed and dotted lines for different NE/SSE-interface electrical resistances. Then, the grey regions shown in Fig. 5(b) and Fig. 5(c) represent the areas of $K_I^{(cfp)} < \xi K_{IC} - K_I^{(ts)}$ where the d/c remains stable and stationary under the applied current density i^{∞}, for the NE and PE cooling configurations, respectively. The two U-TCD diagrams are convenient to visualize variations of $K_I^{(ts)}$, $K_I^{(cfp)}$, a, and i_{TCD}^{∞} at the critical onset state of an SSE's d/c growth for given SSE properties, and useful for finding high dendrite-growth resistance (DGR) as will be discussed in the following section. The total DGR (t-DGR) is composed of resistance against the field concentration of a d/c-tip characteristic field (fc-DGR) and resistance against d/c growth kinetics in the d/c-tip characteristic field (gk-DGR), through multiplication. For simplicity, we refer to 'DGR' as the fc-DGR, and use 'ET-factor' to characterize the gk-DGR in the rest of this paper.

5. Discussions

As analyzed in previous sections, d/c-tip advancement is driven by long-range interactions. The electrode potential affects the localized process through electrical potential, ion flow, stress, and temperature fields in solid-state electrolytes (SSEs). These long-range interactions generate a nominal stress intensity factor that governs localized d/c-tip advancement. The ability of these interactions to produce this nominal stress intensity factor determines the nominal DGR of SSEs, while the effectiveness of this factor in initiating d/c-tip advancement is described by the ET factor ξ. In the following subsections, we discuss how the nominal DGR and the ET factor are represented on the U-TCD, and how they can be improved, measured, and used for studying high-DGR fast-charging batteries. In this paper, the DGR implies the nominal dendrite growth resistance without dendrite yielding.

5.1. ***On Universal Threshold Current Density Diagram*** **(U-TCD)**: As discussed above, Eq. (22) sets parabolic limit curves. The convex black dashed curve A-B in Fig. 5(b) represents the limit for NE cooling for both straight and traction-free SSE films. In contrast, for PE cooling, the concave black dashed curve in Fig. 5(c) is for a straight SSE film while the concave dotted curve corresponds to a traction-free film. These limit curves represent the TCDs for d/c growth in SSEs on the normalized $\left(i^{\infty}/i_{ch}\,, K_I/K_{IC}\right)$ plane of the U-TCD diagrams shown in Figs. 5(b) and (c). For these illustrations, ξ was chosen, as an example, to be 0.58. This value is based on the theoretical prediction of a Li-dendrite/LLZO interface energy toughened by KF doping (Zhang et al., 2024).

Three straight lines $0\text{-}C_1$, $0\text{-}C_2$, and $0\text{-}C_3$ in Fig. 5(b) correspond to Eq. (19) on the U-TCD diagram for $a = 1{,}10$, and $100\mu m$ respectively. The red dashed line of $K_I/K_{IC} = \xi$ would be the TCD limit line for athermal (or isothermal) analysis prediction (Mukherjee et al., 2023). For example, the athermal analysis predicts that d/c would start to grow at the state of F on the U-TCD diagram. However, the current thermomechanical analysis ensures the onset of $10\mu m$ d/c growth at C_2 for the NE cooling. It is surprising that the thermal effect is significant on TCD with only a few degrees (4.3K) overall variation in the LLZO SSE. Our thermomechanical analysis predicts d/c-tip states of $(i^{\infty}/i_{ch}^{\pm}\,, K_I^{(cfp)}/K_{IC})$ within the limit curve. This is depicted as a grey region in

Fig. 5(b), and these states are stable and stationary for all admissible d/c lengths for the NE cooling. We plotted intersection points of Eq. (19) and Eq. (22) curves for various d/c lengths ($a = 10, 100, 150, 200, 500, 800\ \mu m$) for four different SSEs: lithium lanthanum zirconium oxide (LLZO), lithium phosphorus sulfur chloride (LPSCl), lithium aluminum titanium phosphate (LATP), and lithium phosphorus oxynitride (LiPON). All the data points for these SSEs lie on the universal limit curve, but at different locations for the same d/c lengths. This reflects different DGRs for different SSEs. Mukherjee D et al. (2023) conducted an athermal analysis of undoped LLZO, which is illustrated as a red dash-dot line of $\xi = 0.12$ in Fig. 5(b). Their analysis identified the TCD points R_1, R_2, and R_3 for $a = 50, 10$, and $1\ \mu m$ on the U-TCD diagram in the same figure. In contrast, our thermomechanical analysis identified points $C_2^{'}$ and $C_3^{'}$ on the diagram, corresponding to points R_2, and R_3. Thermal effects on the d/c with a length of 50 μm are negligible at point R_1.

Figure 5(c) shows the U-TCD for PE cooling. As the PE-cooling limit curves are concave up, PE-cooling TCDs are much larger than those of NE-cooling TCDs for the same d/c length. Since the ion current generates heat at the NE/SSE interface due to finite interface electrical resistance, the temperature gradient at the SSE side of the interface is finite for the primary PE cooling configuration. For PE cooling, the near-interface temperature gradient influences the thermal stress intensity factor at the d/c tip. Thus, TCD limit curves in Fig. 5(c) are shown separately for different interface electrical resistances. The dashed limit curve of $\xi = 0.58$ in Fig. 5(c) represents the case where the same interface resistance value of LPSCl, specifically 5 Ω·cm² (Sharafi et al., 2017a), was used for different SSEs. In addition, an interface resistance value of 50 Ω·cm² was tested to see the dependence of the limit curve on the interface resistance; this result is shown as a dotted curve. The chained curve in Fig. 5(c) corresponds to $\xi = 0.12$, as for that in Fig. 5(b). The U-TCD limit curves in Fig. 5(b) and (c) show that PE cooling substantially increases the DGR. For LLZO under PE-cooling, the DGR diverges for a d/c length shorter than 8 μm in this framework of linear thermo-elastic analysis. For this diverging DGR case, the DGR would be limited by nonlinear electro-chemo-thermo-mechanical responses of the SSE.

5.2. *On Dendrite Growth Resistance* (DGR): Next, we consider DGRs, $R_{dg}^{(l)}$ and $R_{dg}^{(s)}$, of a long and a short d/c's, respectively. Since Eq. (18) expresses i_{TCD}^{∞} as a function of a, we take the long d/c limit of Eq. (18) for $\Lambda_2 Z^2 i_0^2 a^{-3/2} \xi K_{IC} \ll 1$ and obtain

$$i_{TCD}^{\infty(l)\pm} = \left(\frac{1}{\sqrt{\pi}\beta a^{3/2}}\right) R_{dg}^{(l)} \xi \tag{23a}$$

where

$$R_{dg}^{(l)} = \frac{V_m \kappa^{ion} K_{IC}}{zF} \tag{23b}$$

The parentheses term in Eq. (23a) is purely a geometrical factor of the d/c configuration for the long d/c limit TDC. Equation (23a) shows that $i_{TCD}^{\infty(l)}$ is inversely proportional to $a^{3/2}$, and proportional to $R_{dg}^{(l)}$ and the ET-factor, ξ. Equation (23b) reveals that $R_{dg}^{(l)}$ represents DGR against crack-face loading, which is athermal and proportional to the lithium property $(zF/V_m)^{-1}$, and the SSE properties, κ^{ion} and K_{IC}. Equations (23a & b) describe the TDC behavior near the point A (or A') on the U-TCD diagram in Fig. 5(b). In contrast, taking the short d/c limit of Eq. (18) for $\Lambda_2 Z^2 i_0^2 a^{-3/2} \xi K_{IC} \gg 1$, we get the short-d/c-limit TDC,

$$i_{TCD}^{\infty(s)+} = \left(\frac{1}{\sqrt{\gamma_+}(\pi a)^{1/4}}\right) \frac{1}{W} R_{dg}^{(s)} \sqrt{\xi} \tag{24a}$$

where

$$R_{dg}^{(s)} = \sqrt{\frac{\kappa^{th} \kappa^{ion} K_{IC}}{\alpha E^*}} \tag{24b}$$

Equations (24a & b) depict the TDC behavior near the point B (or B') on the U-TCD diagram in Fig.5(b). The parentheses term and $1/W$ in Eq. (23a) are purely a geometrical factors of the d/c configuration for short-d/c-limit TDC. Equation (24a) indicates that $i_{TCD}^{\infty(s)}$ is inversely proportional to $a^{1/4}$, and proportional to $R_{dg}^{(s)}$ and the square root of the ET-factor, ξ. Equation (24b) discloses

that SSEs have higher short-d/c-limit DGR for higher thermal conductivity and ion conductivity, and for lower thermal expansion coefficient and Young's modulus.

5.3. ***On Dendrite/Crack nucleation***: TDC is a monotonically decreasing function of a in Eq. (18) and Eq. (24a). Once a d/c is nucleated at a critical nucleation length $a = a_{cr}^{(nu)}$, the dendrite growth becomes unstable under constant i^{∞}, within a time scale limited by thermal diffusion and kinetic Li-deposition processes. Equations (24a & b) show that the d/c nucleation TCD, $i_{TCD}^{\infty(nu)}$, is determined by an extrinsic geometry parameter W, three semi-intrinsic d/c-growth parameters, $a_{cr}^{(nu)}, \xi,$ and K_{IC}, and four intrinsic material-property parameters, $\kappa^{ion}, \kappa^{th}, \alpha,$ and E^*. High $\xi, K_{IC}, \kappa^{ion}, \kappa^{th}$, and low $W, a_{cr}^{(nu)}, \alpha, E^*$ elevate the dendrite-nucleation TDC, $i_{TCD}^{\infty(nu)}$, of an SSE. The thinner the SSE, the higher $i_{TCD}^{\infty(nu)}$. Grain sizes, grain-boundary properties, and grain-boundary or interface dopants of SSEs can typically modify the semi-intrinsic d/c-growth parameters, $a_{cr}^{(nu)}, \xi,$ andK_{IC}. Atomic compositions, crystal structures, and bulk dopants typically determine the intrinsic material-property parameters $\kappa^{ion}, \kappa^{th}, \alpha,$ and E^*.

In search of new effective SSEs, numerous SSEs of various atomic compositions and crystal structures have been developed (Song et al., 2026, Sakuda et al., 2013, Cai et al., 2024, Herbert et al., 2011, Hu et al., 2021, Yan et al., 2021, McGrogan et al., 2017, Chen et al., 2025, Wolfenstine et al., 2017, Cheng et al., 2021, Singh et al., 2022, Kim et al., 2022, Hupfer et al., 2016, Tian et al., 2019, Bock et al., 2020, Wang et al., 2024, Baba and Kawamura, 2016, Shi et al., 2023a, Shi et al., 2023b, Wang et al., 2018, Wang et al., 2025, Kwatek et al., 2020, Hubaud et al., 2015, Song et al., 2025, López-Aranguren et al., 2021, Jagannadham, 2016, Papakyriakou et al., 2021, Matijasevic et al., 2021, Minafra et al., 2020, Yu et al., 2015, Shao et al., 2016, Sahal et al., 2023, Pharr et al., 1992, Wolfenstine et al., 2013, Sastre et al., 2020). Among them, intrinsic material properties $\kappa^{ion}, \kappa^{th}, \alpha, E, \nu,$ and a semi-intrinsic d/c-growth parameter, K_{IC}, of typical seven SSEs are tabulated in Table 1. The other two material parameters that affects $i_{TCD}^{\infty(nu)}$ are $a_{cr}^{(nu)}$ and ξ. The d/c nucleation length parameter $a_{cr}^{(nu)}$ heavily depends on the NE/SSE interface morphology, the SSE grain characteristics, and the electrochemical reaction chemistry at the interface. The ET factor ξ is influenced by the near d/c-tip grain boundary mechanisms of electron leaking for Li

island formation (Pustorino et al., 2024) and micro-crack toughening processes (Zhang et al., 2025). Besides $a_{cr}^{(nu)}$ and ξ, we evaluated and tabulated Z and $R_{dg}^{(s)}$ in Table 2 to show how the five material properties influence the DGR of the seven SSEs. The critical ion-current density for dendrite nucleation is proportional to $R_{dg}^{(s)}$ and $\sqrt{\xi}$, and inversely proportional to W and approximately $\left(a_{cr}^{(nu)}\right)^{1/4}$.

5.4. ***On Long-Range Interactions in DGR***: The semi-intrinsic material properties of SSEs are influenced by manufacturing processes. In contrast, the intrinsic properties reported in the literature tend to be more uniform among different samples. Therefore, the DGR, $R_{dg}^{(s)}$, can be used to establish a DGR hierarchy amongst different SSEs. Among the seven SSEs considered, LPSCl exhibits the highest $R_{dg}^{(s)}$ due to its very low Young's modulus and high ionic conductivity, despite its low fracture toughness and high thermal expansion coefficient. The SSE with the next highest $R_{dg}^{(s)}$ is LAGP, which benefits from a very low thermal expansion coefficient and relatively high thermal conductivity, although it has low ionic conductivity. The addition of Tantalum to LLZO significantly enhances its $R_{dg}^{(s)}$ primarily by improving thermal conductivity. LiPON, an amorphous SSE, surpasses LLZO in $R_{dg}^{(s)}$ due to its high toughness, very high thermal conductivity, and relatively low thermal expansion coefficient. In contrast, LLTP has a lower $R_{dg}^{(s)}$ value largely because of its high thermal expansion coefficient and low thermal conductivity. Finally, LPS-glass has a low $R_{dg}^{(s)}$ value mainly due to its very low ionic conductivity and high thermal expansion coefficient. SSEs with favorable thermal properties for a higher $R_{dg}^{(s)}$ value have generally been reported as chemically stable. As observed in the seven SSEs, the DGRs of different SSEs can be enhanced by various mechanisms. These mechanisms include providing favorable properties such as ion conductivity, thermal conductivity, thermal expansion coefficient, elastic modulus, and fracture toughness. Ion and thermal conductivities depend on the crystal structures, which give advantageous density distributions of phonon states for ion and heat conduction. Thermal expansion coefficient, elastic modulus, and fracture toughness are determined primarily by anharmonicity, stiffness, and stability of interatomic bonding, respectively. High DGR SSEs can

be developed by designing proper SSE lattice structures that offer advantageous intrinsic properties and combinations thereof.

In the above, although the five material properties involved in $R_{dg}^{(s)}$ were regarded as relatively uniform among different samples for the sake of discussion, we anticipate that the SSE properties have some variability depending on their porosities, grain sizes, and residual stresses. Additionally, these properties also depend on their measurement or evaluation methods used. For example, the thermal expansion coefficient measured with an atomic-lattice-based method like XRD (Matijasevic et al., 2021, Wang et al., 2024, Hubaud et al., 2015, Hupfer et al., 2016) is overestimated compared to that obtained with a direct strain measurement method such as multi-beam optical stress sensor (MOSS) (Cai et al., 2024, Song et al., 2026) as shown for LLZTO in Table 1. The α values cited in Table 1 are based on neutron diffraction for LPSCl (Minafra et al., 2020); XRD for LAGP (Matijasevic et al., 2021), LLZTO (Wang et al., 2024), LLZO (Hubaud et al., 2015), and LATP (Hupfer et al., 2016); MOSS for LLZTO (Song et al., 2026) and LiPON (Cai et al., 2024); DFT-MD for LPS glass (Baba and Kawamura, 2016). Although the variability of the LLZTO values measured with XRD and MOSS is evident, it does not alter the hierarchy order as shown in Table 1.

5.5. ***On the Toughness of Electro-Chemically Active SSE*** : Equations (24a & b) show that $i_{TCD}^{\propto(s)+}$ is proportional to $\sqrt{\xi K_{IC}}$, where ξK_{IC} represents the toughness of an electro-chemically active SSE with the purely mechanical toughness K_{IC} of the SSE in the inactive state. The toughness is typically measured by nanoindentation, while ξK_{IC} could not be measured consistently. Regarding the measurement of ξK_{IC}, we consider a general temperature distribution in an SSE under simultaneous cooling from both NE and PE sides, as shown in Fig. 6(a4). The temperature distribution is given by Eq. (A1) in the Appendix. The peak temperature is located at $x_1 = W_e < W$ for a general both-side cooling as depicted in Fig. 6(a4), and can be derived from (A1) as

$$W_e = \frac{\kappa_{th}\kappa_{ion}(\theta_W - \theta_0)}{(i^\infty)^2 W} + \frac{W}{2} \tag{25a}$$

Here, W_e is an effective thickness of SSE under both-side cooling, which is equivalent to the SSE thickness of NE cooling, shown in Fig. 6(a1), for their temperature profiles. Inserting the expression of W_e in Eq. (25a) into the thickness W in Eqs. (24a & b), we get an expression,

$$(\theta_W - \theta_0)_{cr} = \frac{\xi K_{IC}}{2\alpha E^* \gamma_+ \sqrt{\pi a}} \tag{25b}$$

for a short d/c of length $a \ll W_e$. By measuring the critical temperature difference between PE and NE for the onset of d/c growth, we can get the toughness of the electro-chemically active SSE, ξK_{IC}, using Eq. (25b). This measurement method will help address the high χ_{ts}-number growth of a short d/c under high ionic current density, as it is technologically vital for critical d/c growth initiation during fast charging. Furthermore, the quantitative measurement of the ET-factor ξ will be particularly helpful in studying the nano- and micro-mechanisms of SSE toughening against d/c growth. The measurement will clarify material degradation mechanisms that depend on current history (Han et al., 2019) and test the validity of computational predictions (Tian et al., 2019). The study is critically needed in developing high DGR SSEs by designing material structures from an atomic scale to a microstructural scale.

5.6. ***On High-DGR Battery Packing***: In previous sections, DGRs in SSEs have been found to be sensitive to the cooling direction in SSEs. Schematics of parabolic temperature profiles in an SSE are presented in Fig. 6(a1) for NE cooling, 6(a2) for PE cooling, 6(a3) for symmetric cooling, and 6(a4) for asymmetric cooling. Figure 6(b1) illustrates a schematic of thin-film battery packaging for NE cooling of high-capacity, low-voltage batteries. Figures 6(b2) and 6(c) illustrate the schematics of packing for PE cooling in high-capacity, low-voltage batteries. Figure 6(d) illustrates a schematic of bipolar battery packing for PE-side cooling in low-capacity, high-voltage applications. Our study results show that PE-side cooling results in high DGR, particularly for short d/c's that originate from flaws at the NE/SSE interface. Insulation boundary conditions for NE and PE cooling are achieved by unit mirror-symmetry packing of thin battery film pairs in series, as shown in Fig. 6(b1) and 6(b2). Alternatively, they are achieved by separating thin battery films stacked in the same direction with a thin sheet of an insulator, as shown in Fig. 6(c). Bipolar packing can utilize heat flow from neighboring cells to enhance DGR.

Besides controlling the thermal and the cfp stress intensity factors, $K_I^{(ts)}$ and $K_I^{(cfp)}$ with heat flow directions, using nonplanar geometries of battery packing can further augment DGR. For example, a battery roll, as shown in Fig. 6(c), can be an effective solution. Augmentation is achieved by controlling $K_I^{(ext)}$, which is induced by ion-current Joule heating, which would generate a self-regulating contact pressure at the inner boundary of a low-thermal-expansion casing. Normal

stacking pressure on planar thin-film battery packing hardly improves DGR. In contrast, lateral pressure substantially increases DGR. However, it can also cause buckling and splitting delamination in thin-film batteries. External pressure on a rolled battery, on the other hand, partly converts into in-plane lateral pressure, which boosts the DGR of the battery without causing battery-film delamination. Curvature changes and strains in SSE, caused by heat flow and used to self-regulate battery DGR, are provided in the Appendix..

Conclusion

In this paper, we present a thermo-mechanical analysis of dendrite growth resistance in SSEs. Through the analysis, we constructed a universal threshold current density (U-TCD) diagram, one for NE and the other for PE cooling of a thin-film SSE. The construction is based on our experimental observations that a preexisting d/c starts to grow at a TCD in an SSE. For the construction, we analyzed the electrical potential, ion flow, temperature, and stress fields of stationary d/c's in primary SSE specimen geometries, and found that the stress and the temperature-gradient fields have $1/\sqrt{r}$ singularities near the d/c tip.

For a stationary d/c, ion deposition at the dendrite/SSE interface is stagnant and the interface overpotential balances the crack face pressure (cfp) of the d/c. The overpotential does not allow electric-potential or ion-flow focusing singularities at a stationary d/c tip. Instead, the crack face pressure generates stress-field focusing singularity of a cfp stress intensity factor $K_I^{(cfp)}$, and the thermal-conductivity jump across the dendrite/SSE interface promotes temperature-gradient-field focusing singularity at the d/c tip.

Our extended J integral applied to a heat-generating thermoelastic field revealed that the Irwin relation (Irwin, 1957) is asymptotically valid at the d/c tip. However, the heat energy directly released through the singular temperature-gradient field caused by the configuration motion of the d/c tip vanishes at the d/c tip. Instead, the singular temperature-gradient field yields a stress singularity through thermal expansion, characterized by a thermal stress intensity factor $K_I^{(ts)}$at the d/c tip. Then, the $K_I^{(ts)}$ field, together with the $K_I^{(cfp)}$ and $K_I^{(ext)}$ fields, releases energy at the d/c tip during d/c growth.

Analyzing the dendrite-growth criticality with $K_I^{(ts)}$, $K_I^{(cfp)}$, and $K_I^{(ext)}$, we identified material properties that govern the DGR of SSEs. For a long d/c, TCD is inversely proportional to $a^{3/2}$ for a the d/c length, and proportional to the long-d/c DGR, $R_{dg}^{(l)}$. The DGR represents an athermal DGR against crack-face loading, which is proportional to the SSE properties, κ^{ion} and K_{IC}, and does not depend on the SSE thickness. For a short d/c, if the metal dendrite does not yield, TCD is inversely proportional to $a^{1/4}$ and the thickness, W, and proportional to the short-d/c DGR, $R_{dg}^{(s)}\left(=\sqrt{\frac{\kappa^{th}\kappa^{ion}K_{IC}}{\alpha E^*}}\right)$.

The short d/c DGR is technologically important because it determines the flaw sensitivity of SSE TDC. SSEs exhibit higher $R_{dg}^{(s)}$ with higher thermal and ion conductivities, and with lower thermal expansion coefficient and Young's modulus. $R_{dg}^{(s)}$indicates how well the SSE limits the thermal stress focusing at the d/c tip. We surveyed seven SSEs, and the favorable level of $R_{dg}^{(s)}$ for limiting the field focusing depended on various combinations of the five properties.

Besides the DGR that limits field focusing, d/c growth is also resisted by the d/c tip toughness of the chemically active SSE. We define the ET factor, ξ, as the ratio of the d/c-tip fracture toughness of the electrochemically active SSE to that of the inactive SSE. We then demonstrated that the TCD is proportional to ξ for the long d/c limit and to $\sqrt{\xi}$ for the short d/c limit, if the metal dendrite does not yield.

As an application of the thermo-mechanical analysis of SSE, we revealed that the DGR of thin-film SSE is extremely sensitive to the heat flow direction in the SSE. PE cooling substantially increases the SSE TCD. Furthermore, the heat-flow direction and battery-film curvature control provides the design strategy of thin film battery packing for high-DGR self-regulation.

Ethics statement. This did not involve any data related to human or animals.

Data accessibility. This article has no additional data.

Competing interests. We have no competing interests.

Authors' contributions. All six coauthors participated in conceiving the battery modeling, interpreting the results, and drafting the manuscript through regular weekly research meetings. CG and SS carried out the FEM analysis, and the experiments with ZY. BS and PG supervised the experimental work, and KSK supervised the mathematical modeling and FEM simulation work. All authors gave final approval for the publication.

Funding statement. CG and BWS acknowledge support from NSF, Award DMR – 2124775, SS and PG from ONR, Award N00014-21-1-2815, and PG and KSK from Brown University, Award ISE – GR300378.

Acknowledgements. Valuable discussions with L. Caretta and Y. Qi are gratefully acknowledged.

4. Appendix: Curvature and stretch strain of a traction-free SSE film caused by ion current

The solution of the heat conduction equations, Eqs. (5) and (6), for uniform ion current density, i^{∞}, for general surface cooling, is given as

$$\theta - \theta_0 = -\frac{(i^{\infty})^2}{2\kappa_{th}\kappa_{ion}} x_1^2 + \left\{\frac{\theta_W - \theta_0}{W} + \frac{(i^{\infty})^2 W}{2\kappa_{th}\kappa_{ion}}\right\} x_1 \tag{A1}$$

where θ_0 and θ_W denote the temperature at $x_1 = 0 and W$, respectively. Subsequently, kinematically admissible linear thermoelastic strains are expressed in terms of the bending curvatures can be expressed in terms of the bending curvatures, K_2 and K_3, and the stretch strains, ε_{22}^0 and ε_{33}^0, as

$$\varepsilon_{22} = -K_3\left(x_1 - \frac{W}{2}\right) + \varepsilon_{22}^0 \tag{A2a}$$

$$\varepsilon_{33} = -K_2\left(x_1 - \frac{W}{2}\right) + \varepsilon_{33}^0 \tag{A2b}$$

Thereafter, stress components $\sigma_{22}(x_1)$, $\sigma_{33}(x_1)$, and strain $\varepsilon_{11}(x_1)$ can be obtained for $\sigma_{11} = \sigma_{kl} = 0$, for $k \neq l$, from the linear thermoelastic constitutive relation,

$$\varepsilon_{ij} = \frac{(1+\nu)\sigma_{ij}}{E} + \left\{-\frac{\nu}{E}\sigma_{kk} + \alpha(\theta - \theta_R)\right\}\delta_{ij} \tag{A3}$$

where θ_R is a reference temperature. Then, for a traction-free film under plane-strain deformation $(K_2 = \varepsilon_{33}^0 = 0)$, no net axial force and no bending moment conditions, $\int_0^W \sigma_{22} dx_1 = \int_0^W x_1\sigma_{22} dx_1 = 0$, result in

$$\varepsilon_{22}^0 = \frac{(1+\nu)\alpha}{2}\left\{\theta_W + \theta_0 - 2\theta_R + \frac{(i^{\infty})^2 W^2}{6\kappa_{th}\kappa_{ion}}\right\} \tag{A4a}$$

$$K_3 = -\frac{(1+\nu)\alpha(\theta_W - \theta_0)}{W} \tag{A4b}$$

For the primary NE cooling of a traction-free SSE film under plane-strain deformation, boundary conditions, $\theta_0 = \theta_R$ and $\left.\frac{d\theta}{dx}\right|_{x_1=W} = 0$, lead to

$$\frac{\theta_W - \theta_R}{W} = \frac{(i^\infty)^2 W}{2\kappa_{th}\kappa_{ion}} \tag{A5a}$$

$$\varepsilon_{22}^0 = \frac{(1+\nu)\alpha(i^\infty)^2 W^2}{3\kappa_{th}\kappa_{ion}} \tag{A5b}$$

$$K_3^{(NEtf)} = -\frac{(1+\nu)\alpha(i^\infty)^2 W}{2\kappa_{th}\kappa_{ion}} \tag{A5c}$$

$$\sigma_{22}^{(NEtf)} = \frac{E\alpha(i^\infty)^2}{2(1-\nu)\kappa_{th}\kappa_{ion}}\left(x_1^2 - Wx_1 + \frac{W^2}{6}\right) \tag{A5d}$$

For the primary NE cooling of a straight SSE film, K_3 vanishes, ε_{22}^0 is the same as $(A5b)$, and the straightening bending stress is added to $(A5d)$ to have

$$\sigma_{22}^{(NEst)} = \frac{E\alpha(i^\infty)^2}{2(1-\nu)\kappa_{th}\kappa_{ion}}\left(x_1^2 - 2Wx_1 + \frac{2W^2}{3}\right) \tag{A5e}$$

In a similar manner, when considering the primary PE cooling of an SSE under plane-strain deformation, boundary conditions, $\theta_W = \theta_R$ and $\left.\frac{d\theta}{dx}\right|_{x_1=0} = 0$, yield ε_{22}^0 the same as $(A5b)$, $K_3^{(PEtf)} = -K_3^{(NEtf)}$, $\sigma_{22}^{(PEtf)} = \sigma_{22}^{(NEtf)}$, and

$$\frac{\theta_0 - \theta_R}{W} = \frac{(i^\infty)^2 W}{2\kappa_{th}\kappa_{ion}} \tag{A6a}$$

$$\sigma_{22}^{(PEst)} = \frac{E\alpha(i^\infty)^2}{2(1-\nu)\kappa_{th}\kappa_{ion}}\left(x_1^2 - \frac{W^2}{3}\right) \tag{A6b}$$

The result shows that the stresses σ_{22}'s caused by Joule heating on both sides of a traction-free SSE film are the same and always tensile, as expressed as $\frac{E\alpha\left(i^\infty\right)^2 W^2}{12(1-\nu)\kappa_{th}\kappa_{ion}}$.

Table 1. Mechanical, electrical and thermal properties of electrolyte materials

Materials	Young's modulus $[GPa]$	Poisson's ratio [-]	Fracture toughness $[MPa\sqrt{m}]$	Ion conductivity $[mS/cm]$	Thermal conductivity $[W/(K \cdot m)]$	Thermal expansion coefficient [E-6/K]
LPSCl	4.7 (McGrogan et al., 2017)	0.37 (McGrogan et al., 2017, Singh et al., 2022)	0.23 (McGrogan et al., 2017, Song et al., 2025)	2.825 (Wang et al., 2018, Shi et al., 2023a)	0.575 (Cheng et al., 2021)	25* (Minafra et al., 2020)
LAGP	125 (Papakyriakou et al., 2021)	0.27 (Cheng et al., 2021)	0.89 (Yan et al., 2021)	0.105 (Wang et al., 2025)	2 (Cheng et al., 2021)	1.78** (Matijasevic et al., 2021)
LLZTO	147 (Yu et al., 2015, Hu et al., 2021)	0.24 (Yu et al., 2015, Hu et al., 2021)	1.5 (Hu et al., 2021)	0.2 (Chen et al., 2025)	1.6 (Cheng et al., 2021, Wang et al., 2024)	11.3† (Song et al., 2026)-17.1** (Wang et al., 2024)
LiPON	77 (Herbert et al., 2011, Pharr et al., 1992)	0.25 (Herbert et al., 2011, Pharr et al., 1992)	2.13 (Sahal et al., 2023)	2.6E-3 (López-Aranguren et al., 2021)	7 (Jagannadham, 2016)	4.1† (Cai et al., 2024)
LLZO	150 (Wolfenstine et al.,	0.26 (Wolfenstine et al.,	1.63 (Wolfensti	0.175 (Shao et al., 2016, Kim et al.,	0.47 (Bock et al., 2020)	13.1** (Hubaud et al., 2015)

	2017, Deng et al., 2015)	2017, Deng et al., 2015)	ne et al., 2013)	2022, Shi et al., 2023b)		
LATP	115 (Wolfensti ne et al., 2017)	0.26 (Deng et al., 2015)	0.89 (Yan et al., 2021)	0.405 (Kwatek et al., 2020)	0.47 (Bock et al., 2020)	31** (Hupfer et al., 2016)
LPS glass	20 (Sakuda et al., 2013)	0.3 (Sakuda et al., 2013)	0.23 (McGroga n et al., 2017)	5.5E-2 (Song et al., 2026)	0.65 (Cheng et al., 2021)	9.5‡ (Baba and Kawamura, 2016)
Note: * Neutron Powder Diffraction method; ** X-ray Diffraction method (XRD); †Multi-beam Optics Stress Sensor (MOSS); ‡ Molecular Dynamics (MD) - Density Functional Theory (DFT) computational method						

Table 2. Calculated material dependent parameters

Materials	Plane-strain modulus $[GPa]$	Z-value $[mA/(cm\sqrt{MPa})]$	DGR $R_{dg}^{(s)}$ $[m^{1/4} \cdot mA/cm]$
LPSCl	5.4	10.9	5.24
LAGP	134.8	2.96	2.79
LLZTO	156.0	1.02 – 1.26	1.25 – 1.54
LiPON	82.1	0.735	1.07

LLZO	160.9	0.627	0.80
LATP	123.3	0.720	0.68
LPS glass	22.0	1.31	0.63

where Z-value is defined as $Z = \sqrt{\frac{\kappa^{ion}{}_{\kappa^{th}}}{\alpha E^*}}$, and DGR value is defined as $Z\sqrt{K_{Ic}}$.

Figure Captions

Fig. 1. Primary SSE specimen geometry with a stationary dendrite/crack: (a) A schematic of an NE cooling configuration of a thin-film SSE with a dendrite/crack, (b) An optical image of dendrite/crack grown out of NE in LLZTO SSE under charging process, (c) A Color map of the difference in principal stresses at the tip of a progressing dendrite in LLZTO, observed by employing the principle of photoelasticity. Stress concentration effect can be observed directly. Adapted with permission from (Athanasiou, Fincher et al. 2024). Copyright 2024 Elsevier Inc.

Fig. 2. FEM analyses of stress and temperature fields near a d/c tip at the critical stress intensity of 0.95 $MPa\sqrt{m}$ in a LLZO SSE under NE cooling in a *straight* ((a)-(c)) and a *traction-free* ((d)-(f)) SSE films: (a)&(d) σ_{yy} distributions near d/c tip regions; three columns for different $\chi_{ts}\left(\equiv K_I^{(ts)}/K_I^{(cfp)}\right)$'s of (1, 10, 100 μm) d/c lengths; three rows for thermal-, cfp-, and total-stress distributions, (b)&(e) σ_{yy} along d/c for different χ_{ts}'s (dotted lines) and $1/\sqrt{r}$fitting (solid lines), (c)&(f) Temperature and temperature gradient along d/c for different χ_{ts}'s.

Fig. 3. FEM analyses of stress and temperature fields near a d/c tip at the critical stress intensity of 0.95 $MPa\sqrt{m}$ in a LLZO SSE under PE cooling in a *straight* ((a)-(c)) and a *traction-free* ((d)-(f)) SSE films: (a)&(d) σ_{yy} distributions near d/c tip regions; three columns for different $\chi_{ts}\left(\equiv K_I^{(ts)}/K_I^{(cfp)}\right)$'s of (1, 10, 100 μm) d/c lengths; two rows for cfp- and total-stress distributions, (b)&(e) σ_{yy} along d/c for different χ_{ts}'s (dotted lines) and $1/\sqrt{r}$fitting (solid lines), (c)&(f) Temperature and temperature gradient along d/c for different χ_{ts}'s.

Fig. 4. Extended J-integral contour and its path independence in an active SSE under NE cooling: (a) A schematic of extended J-integral contour paths and enclosed area$A$, (b) Path dependence of the contour and area integral parts, and path independence of the total extended J-integral.

Fig. 5. Universal threshold current density (U-TCD) diagrams: (a) Shape coefficients of the crack-face-pressure and the thermal stress intensity factors as functions of a normalized d/c length for four different cooling and loading boundary conditions, (b) U-TCD diagram for NE cooling of a straight SSE film, (c) U-TCD diagram for PE cooling of a straight SSE film.

Fig. 6. Thermal-management configurations of ASSB cooling to enhance dendrite growth resistance (DGR): (a) Schematics of temperature profiles in an SSE; (1) NE) cooling, (2) PE

cooling, (3) symmetric cooling, and (4) asymmetric both-side cooling, (b) Battery packaging configurations for (1) negative and (2) positive electrode cooling with mirror-symmetry cell pairs in a parallel circuit. (c) A rolled battery configuration for PE cooling; a thin battery film is self-separated by a grey cooling film and a dot-patterned thermal and electrical insulation film, (d) Bipolar battery packing with PE cooling.

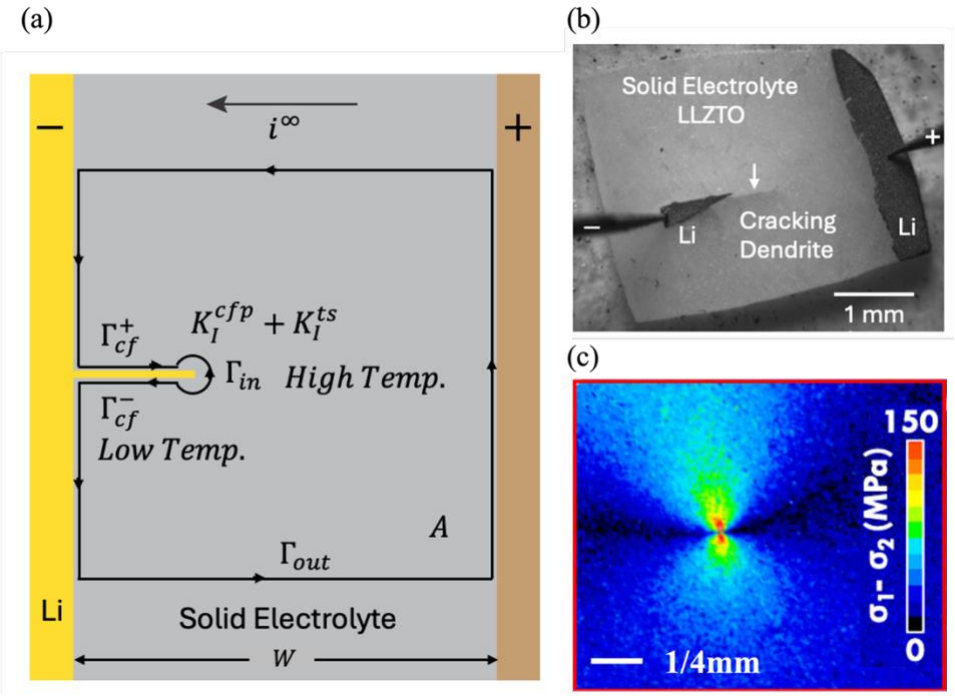
(a)
(b)
(c)
i^{∞}
−
+
Γ_{cf}^{+}
$K_I^{cfp} + K_I^{ts}$
Γ_{in}
High Temp.
Γ_{cf}^{-}
Low Temp.
A
Γ_{out}
Li
Solid Electrolyte
W
Solid Electrolyte
LLZTO
Li
Cracking
Dendrite
Li
1 mm
150
$\sigma_1 - \sigma_2$ (MPa)
0
1/4mm

Fig. 1

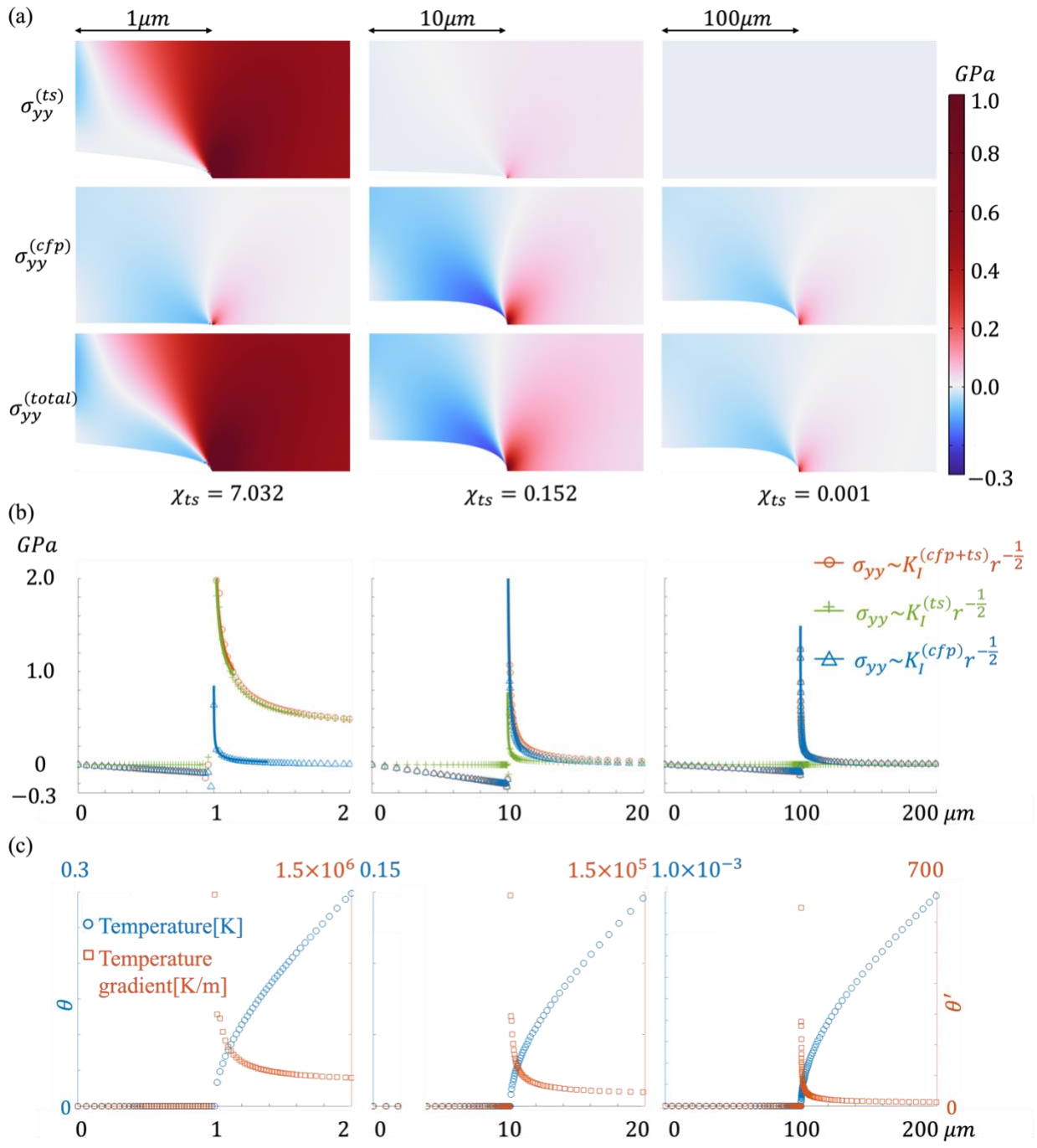
(a)
1μm
10μm
100μm
$\sigma_{yy}^{(ts)}$
$\sigma_{yy}^{(cfp)}$
$\sigma_{yy}^{(total)}$
GPa
1.0
0.8
0.6
0.4
0.2
0.0
−0.3
$\chi_{ts} = 7.032$
$\chi_{ts} = 0.152$
$\chi_{ts} = 0.001$
(b)
GPa
2.0
1.0
0
−0.3
$\sigma_{yy} \sim K_I^{(cfp+ts)} r^{-\frac{1}{2}}$
$\sigma_{yy} \sim K_I^{(ts)} r^{-\frac{1}{2}}$
$\sigma_{yy} \sim K_I^{(cfp)} r^{-\frac{1}{2}}$
0 1 2
0 10 20
0 100 200 μm
(c)
0.3
1.5×10^6
0.15
1.5×10^5
1.0×10^−3
700
Temperature[K]
Temperature gradient[K/m]
θ
θ′
0
0 1 2
0 10 20
0 100 200 μm

Fig2 (a), (b), (c)

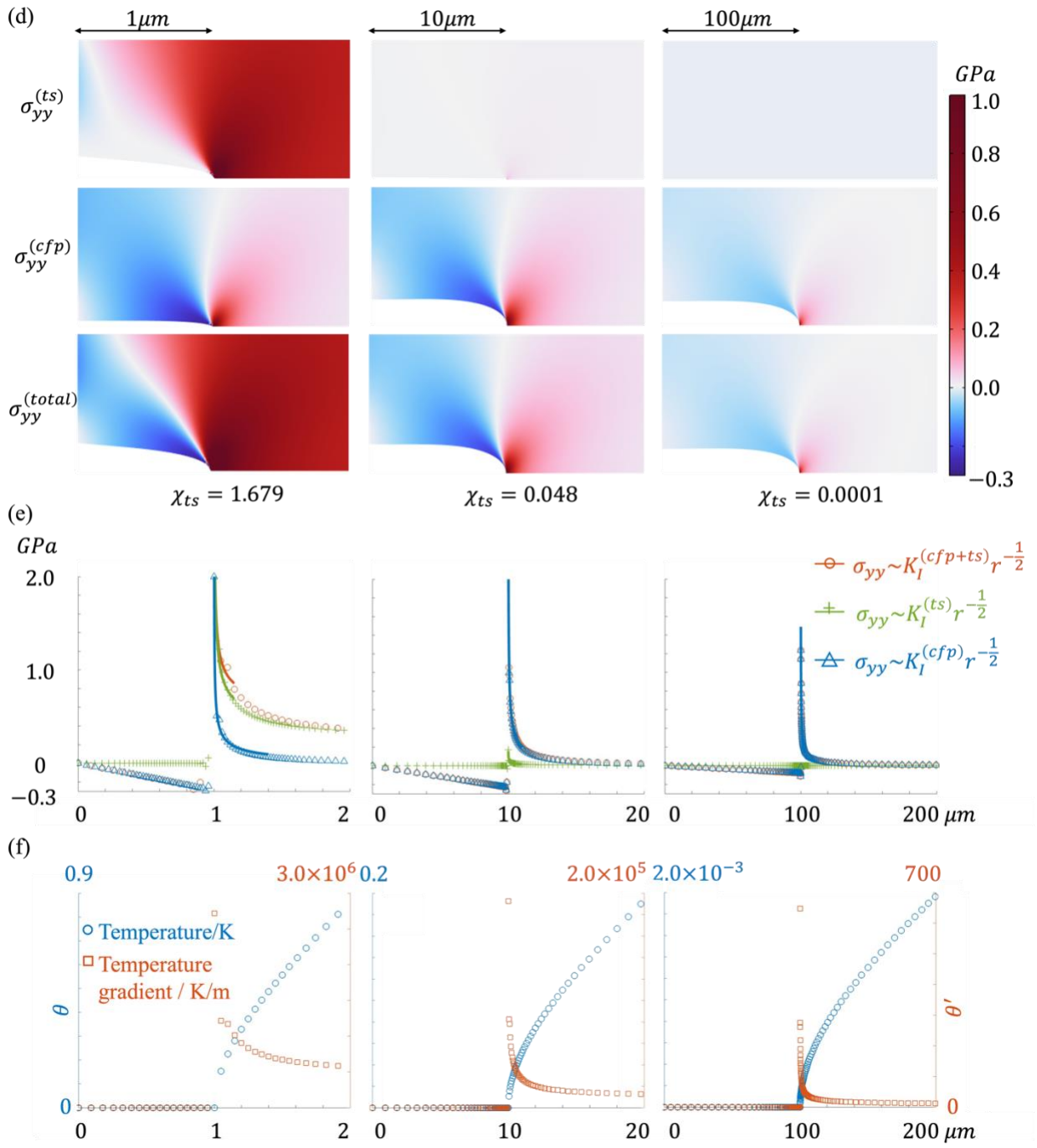
(d)
1μm
10μm
100μm
$\sigma_{yy}^{(ts)}$
$\sigma_{yy}^{(cfp)}$
$\sigma_{yy}^{(total)}$
GPa
1.0
0.8
0.6
0.4
0.2
0.0
−0.3
$\chi_{ts} = 1.679$
$\chi_{ts} = 0.048$
$\chi_{ts} = 0.0001$
(e)
GPa
2.0
1.0
0
−0.3
$\sigma_{yy} \sim K_I^{(cfp+ts)} r^{-\frac{1}{2}}$
$\sigma_{yy} \sim K_I^{(ts)} r^{-\frac{1}{2}}$
$\sigma_{yy} \sim K_I^{(cfp)} r^{-\frac{1}{2}}$
0
1
2
0
10
20
0
100
200 μm
(f)
0.9
3.0×10^{6}
0.2
2.0×10^{5}
2.0×10^{-3}
700
Temperature/K
Temperature gradient / K/m
θ
θ′
0
0
1
2
0
10
20
0
100
200 μm

Fig. 2 (d), (e), (f)

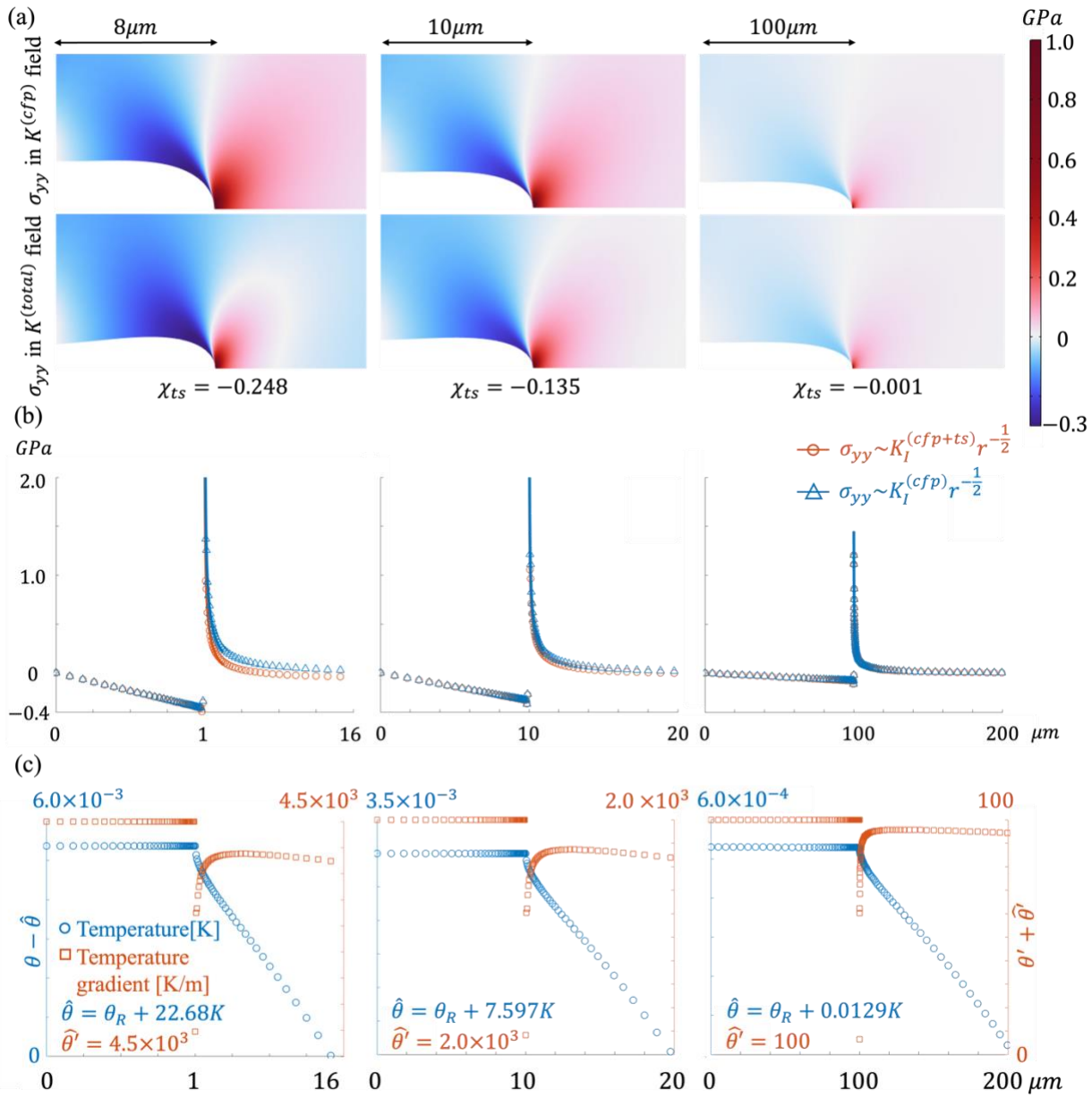
(a)
8μm
10μm
100μm
GPa
1.0
0.8
0.6
0.4
0.2
0
−0.3
σyy in K(cfp) field
σyy in K(total) field
χts = −0.248
χts = −0.135
χts = −0.001
(b)
GPa
σyy~K_I^(cfp+ts) r^−1/2
σyy~K_I^(cfp) r^−1/2
2.0
1.0
0
−0.4
0
1
16
0
10
20
0
100
200 μm
(c)
6.0×10^−3
4.5×10^3
3.5×10^−3
2.0 ×10^3
6.0×10^−4
100
θ − θ̂
θ′ + θ̂′
Temperature[K]
Temperature gradient [K/m]
θ̂ = θ_R + 22.68K
θ̂′ = 4.5×10^3
θ̂ = θ_R + 7.597K
θ̂′ = 2.0×10^3
θ̂ = θ_R + 0.0129K
θ̂′ = 100
0
1
16
0
10
20
0
100
200 μm

Fig. 3 (a), (b), (c)

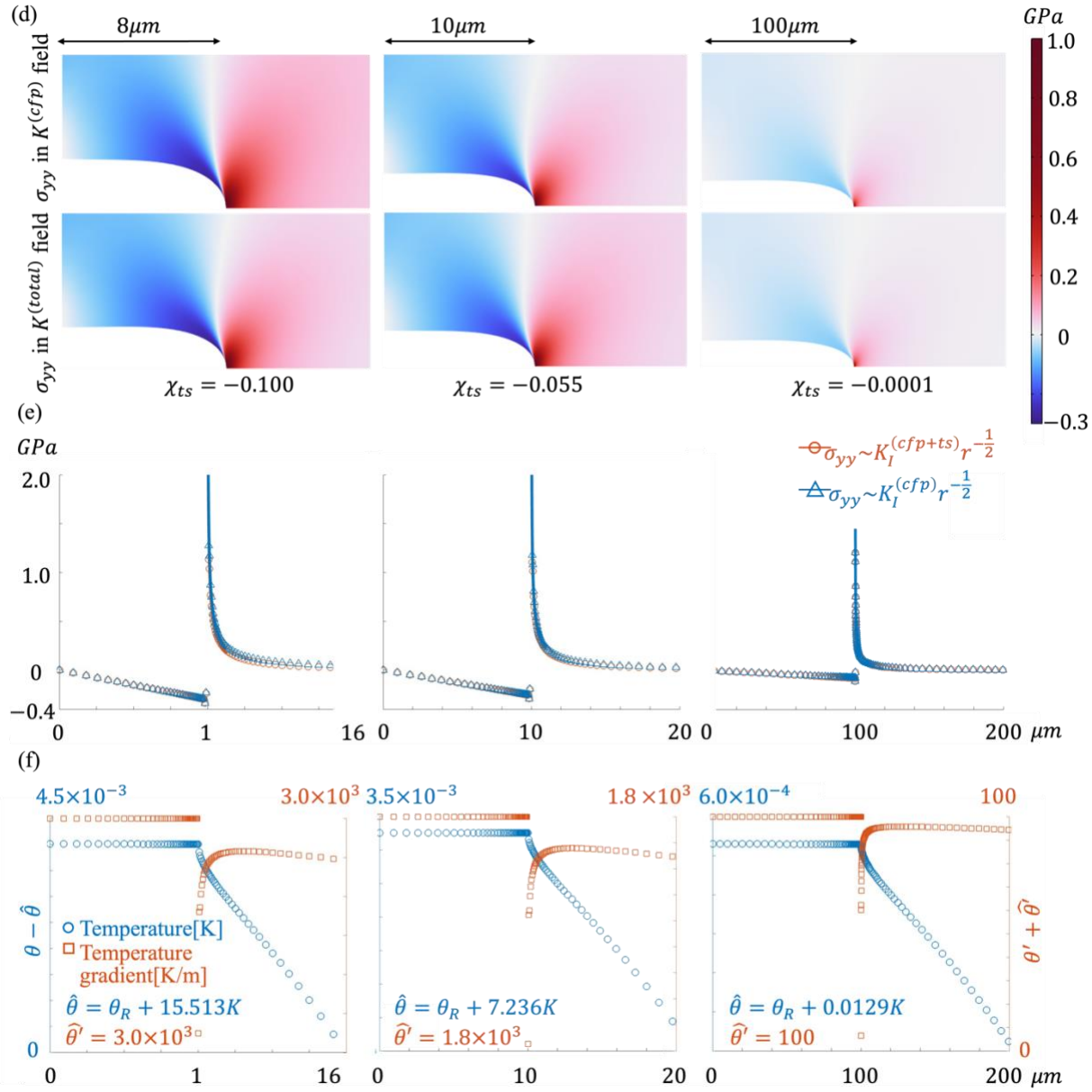
(d)
8μm
10μm
100μm
GPa
1.0
0.8
0.6
0.4
0.2
0
−0.3
σyy in K(cfp) field
σyy in K(total) field
χts = −0.100
χts = −0.055
χts = −0.0001
(e)
GPa
2.0
1.0
0
−0.4
σyy~KI(cfp+ts) r−1/2
σyy~KI(cfp) r−1/2
0
1
16
0
10
20
0
100
200 μm
(f)
4.5×10−3
3.0×10³
3.5×10−3
1.8 ×10³
6.0×10−4
100
θ − θ̂
θ′ + θ̂′
Temperature[K]
Temperature gradient[K/m]
θ̂ = θR + 15.513K
θ̂′ = 3.0×10³
θ̂ = θR + 7.236K
θ̂′ = 1.8×10³
θ̂ = θR + 0.0129K
θ̂′ = 100
0
0
1
16
0
10
20
0
100
200 μm

Fig. 3 (d), (e), (f)

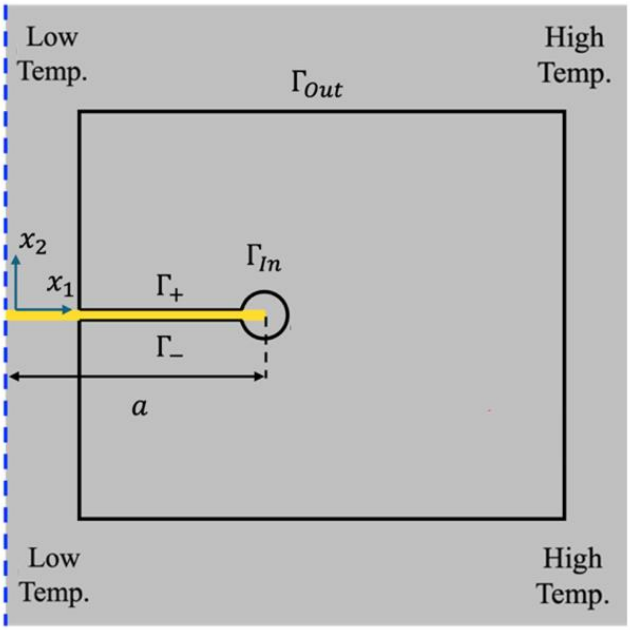
Low
Temp.
High
Temp.
Γ_{Out}
x_2
x_1
Γ_{In}
Γ_+
Γ_-
a
Low
Temp.
High
Temp.

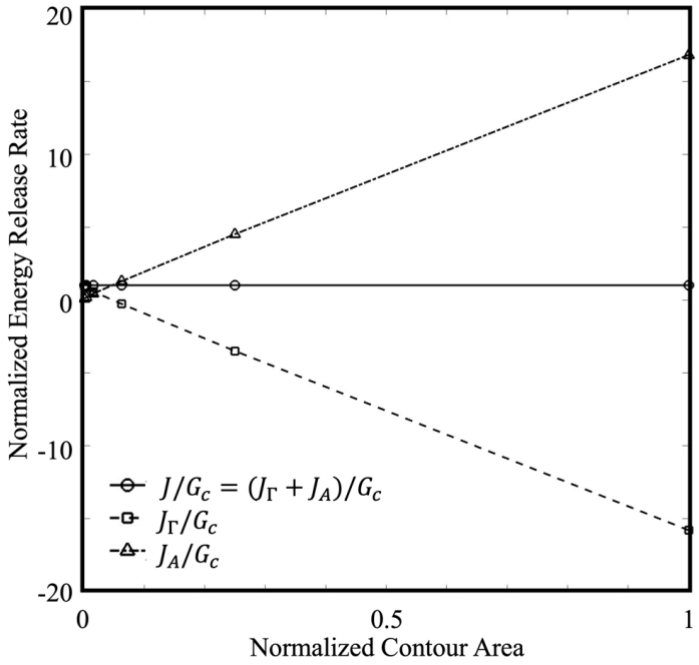
Normalized Energy Release Rate
20
10
0
-10
-20
0
0.5
1
Normalized Contour Area
$J/G_c = (J_\Gamma + J_A)/G_c$
J_Γ/G_c
J_A/G_c

(b)

Fig.4.

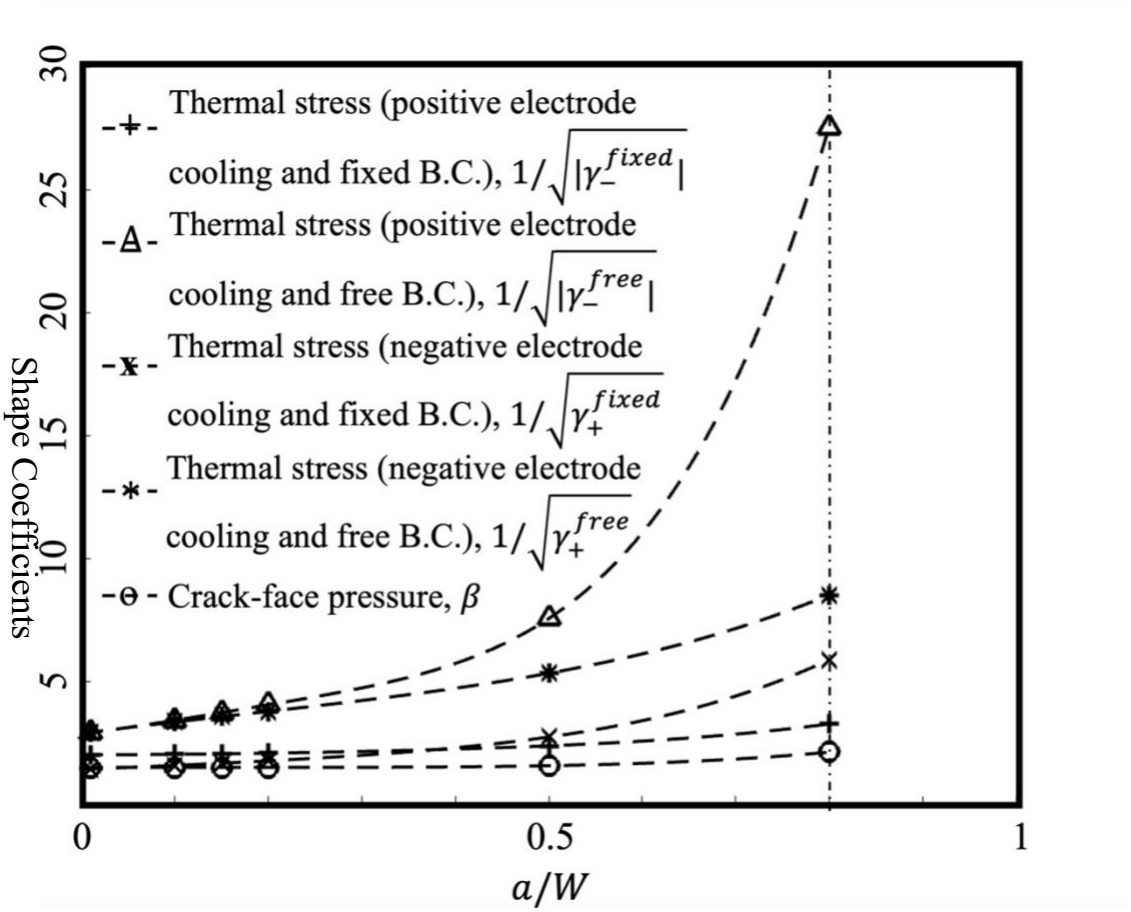
Thermal stress (positive electrode cooling and fixed B.C.), $1/\sqrt{|\gamma_-^{fixed}|}$
Thermal stress (positive electrode cooling and free B.C.), $1/\sqrt{|\gamma_-^{free}|}$
Thermal stress (negative electrode cooling and fixed B.C.), $1/\sqrt{\gamma_+^{fixed}}$
Thermal stress (negative electrode cooling and free B.C.), $1/\sqrt{\gamma_+^{free}}$
Crack-face pressure, β
Shape Coefficients
30
25
20
15
10
5
0
0.5
1
a/W

(a)

Fig. 5

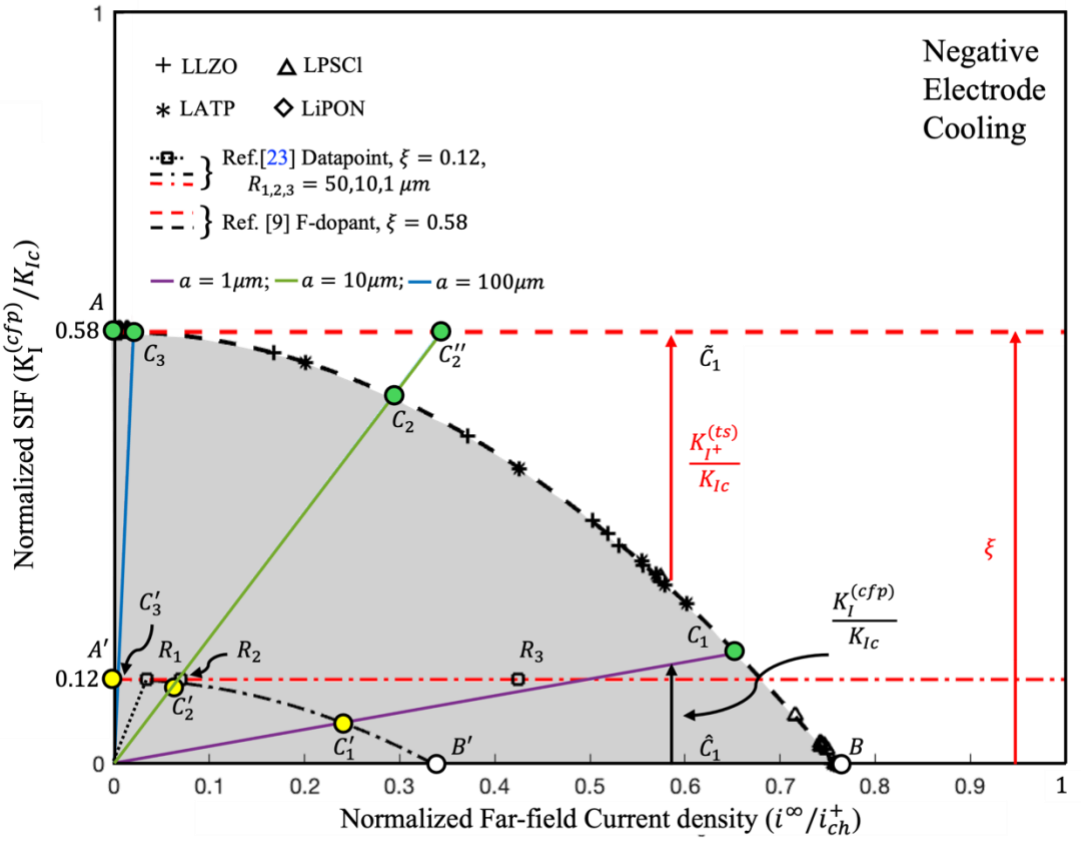
Negative
Electrode
Cooling
LLZO
LPSCl
LATP
LiPON
Ref.[23] Datapoint, $\xi = 0.12$, $R_{1,2,3} = 50,10,1\ \mu m$
Ref. [9] F-dopant, $\xi = 0.58$
$a = 1\mu m$; $a = 10\mu m$; $a = 100\mu m$
Normalized SIF ($K_I^{(cfp)}/K_{Ic}$)
Normalized Far-field Current density (i^{∞}/i_{ch}^{+})
A
A'
B
B'
C_1
C_2
C_3
C_1'
C_2'
C_3'
C_2''
R_1
R_2
R_3
$\tilde{C}_1$
$\hat{C}_1$
$\frac{K_{I^+}^{(ts)}}{K_{Ic}}$
$\frac{K_I^{(cfp)}}{K_{Ic}}$
ξ
0.58
0.12
0
0.1
0.2
0.3
0.4
0.5
0.6
0.7
0.8
0.9
1

(b)

Fig.5.

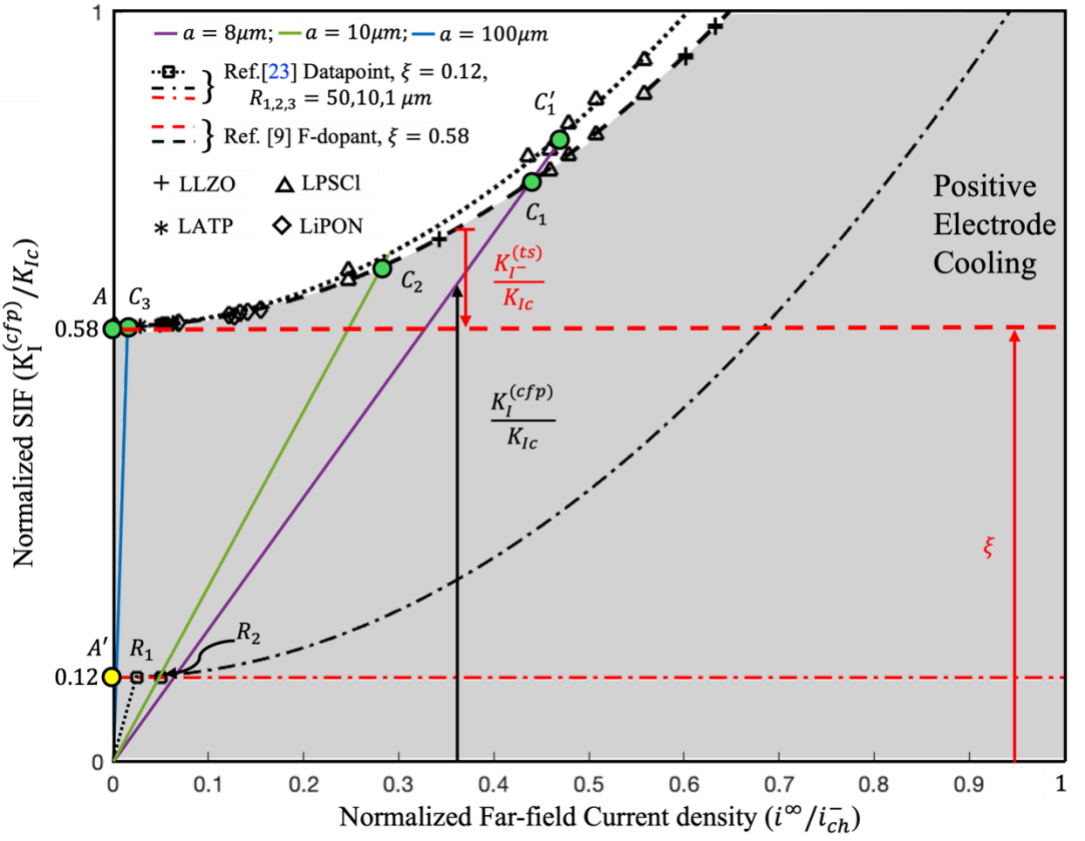
$a = 8\mu m$; $a = 10\mu m$; $a = 100\mu m$
Ref.[23] Datapoint, $\xi = 0.12$, $R_{1,2,3} = 50,10,1\ \mu m$
Ref. [9] F-dopant, $\xi = 0.58$
LLZO
LPSCl
LATP
LiPON
Positive Electrode Cooling
C_1'
C_1
C_2
C_3
A
A'
R_1
R_2
$\frac{K_I^{(ts)}}{K_{Ic}}$
$\frac{K_I^{(cfp)}}{K_{Ic}}$
ξ
0.58
0.12
0
0.1
0.2
0.3
0.4
0.5
0.6
0.7
0.8
0.9
1
Normalized SIF ($K_I^{(cfp)}/K_{Ic}$)
Normalized Far-field Current density (i^{∞}/i_{ch}^{-})

(c)

Fig.5.

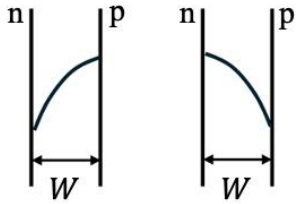

(a1)

(a2)

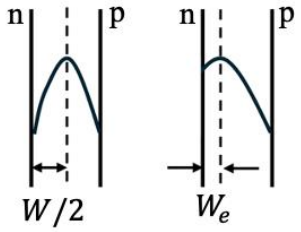

(a3)

(a4)

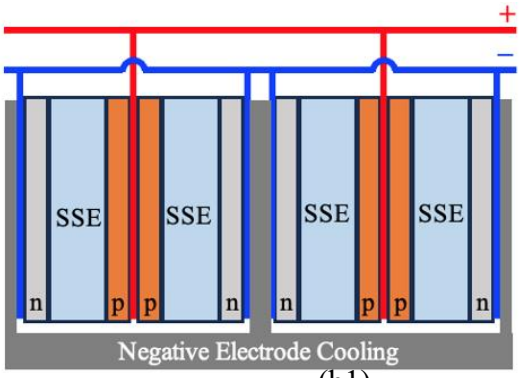

(b1)

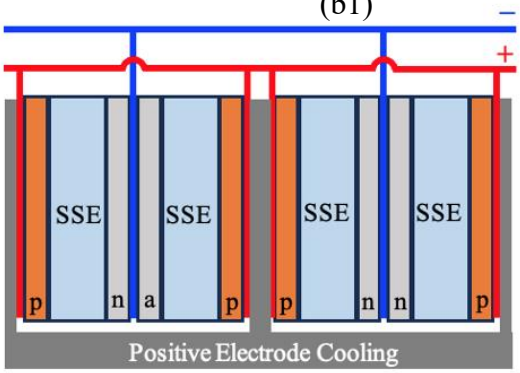

(b2)

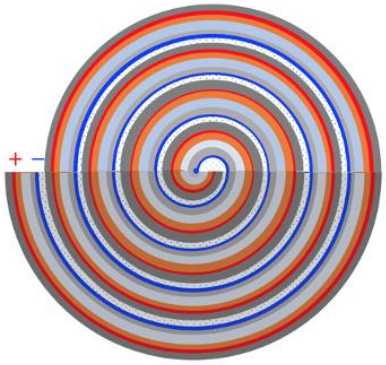

(c)

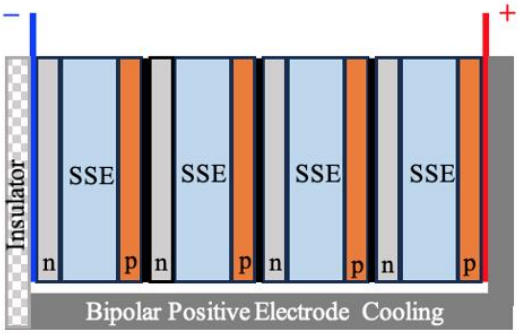

(d)

Fig.6

Reference

ATHANASIOU, C. E., FINCHER, C. D., GILGENBACH, C., GAO, H., CARTER, W. C., CHIANG, Y.-M. & SHELDON, B. W. 2024. Operando measurements of dendrite-induced stresses in ceramic electrolytes using photoelasticity. *Matter,* 7**,** 95–106.

BABA, T. & KAWAMURA, Y. 2016. Structure and Ionic Conductivity of Li2S–P2S5 Glass Electrolytes Simulated with First-Principles Molecular Dynamics. *Frontiers in Energy Research,* 4.

BANKS-SILLS, L. & DOLEV, O. 2004. The conservative M-integral for thermal-elastic problems. *International Journal of Fracture,* 125**,** 149–170.

BOCK, R., ONSRUD, M., KAROLIUSSEN, H., POLLET, B., SELAND, F. & BURHEIM, O. 2020. Thermal Gradients with Sintered Solid State Electrolytes in Lithium-Ion Batteries. *Energies,* 13.

BUTLER, J. A. V. 1924. Studies in heterogeneous equilibria. Part III. A kinetic theory of reversible oxidation potentials at inert electrodes. *Transactions of the Faraday Society,* 19**,** 734–739.

CAI, T., WESTOVER, A., KALNAUS, S., ATHANASIOU, C. E., DUDNEY, N. & SHELDON, B. W. 2024. Thermo-mechanical characterization and stress engineering of Lipon solid electrolyte. *Journal of Materials Chemistry A,* 12**,** 3943–3953.

CHEN, A., LI, N., SUN, C., QIN, Y., QI, L. & BAO, H. 2025. Tailoring particles fineness and Li-ion conductivity of LLZTO solid electrolyte through calcination temperature for solid-state lithium batteries. *Ionics,* 31**,** 6787–6795.

CHENG, Z., ZAHIRI, B., JI, X., CHEN, C., CHALISE, D., BRAUN, P. V. & CAHILL, D. G. 2021. Good Solid-State Electrolytes Have Low, Glass-Like Thermal Conductivity. *Small,* 17**,** e2101693.

COMSOL-INC. COMSOL Multiphysics reference Manual version 5.2.

DENG, Z., WANG, Z., CHU, I.-H., LUO, J. & ONG, S. P. 2015. Elastic Properties of Alkali Superionic Conductor Electrolytes from First Principles Calculations. *Journal of The Electrochemical Society,* 163**,** A67–A74.

ERDEY-GRúZ, T. & VOLMER, M. 1930. Zur Theorie der Wasserstoff Überspannung. *Zeitschrift für Physikalische Chemie,* 150A**,** 203–213.

FINCHER, C. D., ATHANASIOU, C. E., GILGENBACH, C., WANG, M., SHELDON, B. W., CARTER, W. C. & CHIANG, Y.-M. 2022. Controlling dendrite propagation in solid-state batteries with engineered stress. *Joule,* 6**,** 2794–2809.

FINCHER, C. D., GILGENBACH, C., ROACH, C., OSMUNDSEN, R., PENN, A., THOULESS, M. D., CARTER, W. C., SHELDON, B. W., LEBEAU, J. M. & CHIANG, Y. M. 2026. Electrochemical corrosion accompanies dendrite growth in solid electrolytes. *Nature,* 652**,** 906–911.

HAN, F., WESTOVER, A. S., YUE, J., FAN, X., WANG, F., CHI, M., LEONARD, D. N., DUDNEY, N. J., WANG, H. & WANG, C. 2019. High electronic conductivity as the origin of lithium dendrite formation within solid electrolytes. *Nature Energy,* 4**,** 187–196.

HERBERT, E. G., TENHAEFF, W. E., DUDNEY, N. J. & PHARR, G. M. 2011. Mechanical characterization of LiPON films using nanoindentation. *Thin Solid Films,* 520**,** 413–418.

HESS, M. 2018. Temperature-Dependence of the Solid-Electrolyte Interphase Overpotential: Part I. Two Parallel Mechanisms, One Phase Transition. *Journal of The Electrochemical Society,* 165**,** A323–A332.

HO, C. Y., POWELL, R. W. & LILEY, P. E. 1972. Thermal Conductivity of the Elements. *Journal of Physical and Chemical Reference Data,* 1**,** 279–421.

HU, S., XU, P., DE VASCONCELOS, L. S., STANCIU, L., NI, H. & ZHAO, K. 2021. Elastic Modulus, Hardness, and Fracture Toughness of Li6.4La3Zr1.4Ta0.6O12 Solid Electrolyte. *Chinese Physics Letters,* 38.

HUBAUD, A. A., SCHROEDER, D. J., INGRAM, B. J., OKASINSKI, J. S. & VAUGHEY, J. T. 2015. Thermal expansion in the garnet-type solid electrolyte (Li7−Al/3)La3Zr2O12 as a function of Al content. *Journal of Alloys and Compounds,* 644**,** 804–807.

HUPFER, T., BUCHARSKY, E. C., SCHELL, K. G., SENYSHYN, A., MONCHAK, M., HOFFMANN, M. J. & EHRENBERG, H. 2016. Evolution of microstructure and its relation to ionic conductivity in Li1+xAlxTi2−x(PO4)3. *Solid State Ionics,* 288**,** 235–239.

IRWIN, G. R. 1957. Analysis of Stresses and Strains Near the End of a Crack Traversing a Plate. *Journal of Applied Mechanics,* 24**,** 361–364.

JAGANNADHAM, K. 2016. Thermal conductivity and interface thermal conductance of thin films in Li ion batteries. *Journal of Power Sources,* 327**,** 565–572.

JANEK, J. & ZEIER, W. G. 2016. A solid future for battery development. *Nature Energy,* 1.

JIA, Z., SHEN, H., KOU, J., ZHANG, T., WANG, Z., TANG, W., DOEFF, M., CHIANG, C. Y. & CHEN, K. 2024. Solid Electrolyte Bimodal Grain Structures for Improved Cycling Performance. *Adv Mater,* 36**,** e2309019.

KIM, M., PARK, H. G. & PARK, K. 2022. A strategy of enhancing the ionic conductivity of Li(7)La(3)Zr(2)O(12) under accurate sintering conditions. *Phys Chem Chem Phys,* 24**,** 29159–29164.

KWATEK, K., ŚLUBOWSKA, W., RUIZ, C., SOBRADOS, I., SANZ, J., GARBARCZYK, J. E. & NOWIńSKI, J. L. 2020. The mechanism of enhanced ionic conductivity in Li1.3Al0.3Ti1.7(PO4)3–(0.75Li2O·0.25B2O3) composites. *Journal of Alloys and Compounds,* 838.

LóPEZ-ARANGUREN, P., REYNAUD, M., GłUCHOWSKI, P., BUSTINZA, A., GALCERAN, M., LóPEZ DEL AMO, J. M., ARMAND, M. & CASAS-CABANAS, M. 2021. Crystalline LiPON as a Bulk-Type Solid Electrolyte. *ACS Energy Letters,* 6**,** 445–450.

LU, Y., ZHAO, C. Z., YUAN, H., CHENG, X. B., HUANG, J. Q. & ZHANG, Q. 2021. Critical Current Density in Solid-State Lithium Metal Batteries: Mechanism, Influences, and Strategies. *Advanced Functional Materials,* 31.

MANTHIRAM, A., YU, X. & WANG, S. 2017. Lithium battery chemistries enabled by solid-state electrolytes. *Nature Reviews Materials,* 2.

MATIJASEVIC, S., TOPALOVIC, V., GRUJIC, S., SAVIC, V., NIKOLIC, J., LABUS, N. & ZILDZOVIC, S. 2021. The thermophysical properties of primary phase in lithium germanium phosphate glass. *Science of Sintering,* 53**,** 301–310.

MCGROGAN, F. P., SWAMY, T., BISHOP, S. R., EGGLETON, E., PORZ, L., CHEN, X., CHIANG, Y. M. & VAN VLIET, K. J. 2017. Compliant Yet Brittle Mechanical Behavior of Li2S–P2S5 Lithium-Ion-Conducting Solid Electrolyte. *Advanced Energy Materials,* 7.

MERCIER, R., MALUGANI, J.-P., FAHYS, B. & ROBERT, G. 1981. Superionic conduction in Li2S - P2S5 - LiI - glasses. *Solid State Ionics,* 5**,** 663–666.

MINAFRA, N., KRAFT, M. A., BERNGES, T., LI, C., SCHLEM, R., MORGAN, B. J. & ZEIER, W. G. 2020. Local Charge Inhomogeneity and Lithium Distribution in the Superionic Argyrodites Li(6)PS(5)X (X = Cl, Br, I). *Inorg Chem,* 59**,** 11009–11019.

MONROE, C. & NEWMAN, J. 2004. The Effect of Interfacial Deformation on Electrodeposition Kinetics. *Journal of The Electrochemical Society,* 151.

MONROE, C. & NEWMAN, J. 2005. The Impact of Elastic Deformation on Deposition Kinetics at Lithium/Polymer Interfaces. *Journal of The Electrochemical Society,* 152.

MUKHERJEE, D., HAO, S., SHEARING, P. R., MCMEEKING, R. M., FLECK, N. A. & DESHPANDE, V. S. 2023. Ingress of Li into Solid Electrolytes: Cracking and Sparsely Filled Cracks. *Small Structures,* 4.

PAPAKYRIAKOU, M., LU, M., LIU, Y., LIU, Z., CHEN, H., MCDOWELL, M. T. & XIA, S. 2021. Mechanical behavior of inorganic lithium-conducting solid electrolytes. *Journal of Power Sources,* 516.

PHARR, G. M., OLIVER, W. C. & BROTZEN, F. R. 1992. On the generality of the relationship among contact stiffness, contact area, and elastic modulus during indentation. *Journal of Materials Research,* 7**,** 613–617.

PORZ, L., SWAMY, T., SHELDON, B. W., RETTENWANDER, D., FRöMLING, T., THAMAN, H. L., BERENDTS, S., UECKER, R., CARTER, W. C. & CHIANG, Y. M. 2017. Mechanism of Lithium Metal Penetration through Inorganic Solid Electrolytes. *Advanced Energy Materials,* 7.

PUSTORINO, G., JAGAD, H., LI, W., FENG, M., POMA, M., KO, J., JOHARI, P. & QI, Y. 2024. Mechanical and Electronic Properties of Bulk and Surface Li6PS5Cl Argyrodite: First-Principles Insights on Li-Filament Resistance. *Chemistry of Materials,* 37**,** 313–321.

RICE, J. R. 1968. A Path Independent Integral and the Approximate Analysis of Strain Concentration by Notches and Cracks. *Journal of Applied Mechanics,* 35**,** 379–386.

SAHAL, M., MOLLOY, J., NARAYANAN, V. R., LADANI, L., LU, X. & ROLSTON, N. 2023. Robust and Manufacturable Lithium Lanthanum Titanate-Based Solid-State Electrolyte Thin Films Deposited in Open Air. *ACS Omega,* 8**,** 28651–28662.

SAKUDA, A., HAYASHI, A., TAKIGAWA, Y., HIGASHI, K. & TATSUMISAGO, M. 2013. Evaluation of elastic modulus of Li₂S–P₂S₅ glassy solid electrolyte by ultrasonic sound velocity measurement and compression test. *Journal of the Ceramic Society of Japan,* 121**,** 946–949.

SANDOVAL, S. E., HASLAM, C. G., VISHNUGOPI, B. S., LIAO, D. W., YOON, J. S., PARK, S. H., WANG, Y., MITLIN, D., HATZELL, K. B., SIEGEL, D. J., MUKHERJEE, P. P., DASGUPTA, N. P., SAKAMOTO, J. & MCDOWELL, M. T. 2025. Electro-chemo-mechanics of anode-free solid-state batteries. *Nat Mater,* 24**,** 673–681.

SASTRE, J., PRIEBE, A., DöBELI, M., MICHLER, J., TIWARI, A. N. & ROMANYUK, Y. E. 2020. Lithium Garnet Li7La3Zr2O12 Electrolyte for All-Solid-State Batteries: Closing the Gap between Bulk and Thin Film Li-Ion Conductivities. *Advanced Materials Interfaces,* 7.

SHAO, C., LIU, H., YU, Z., ZHENG, Z., SUN, N. & DIAO, C. 2016. Structure and ionic conductivity of cubic Li7La3Zr2O12 solid electrolyte prepared by chemical co-precipitation method. *Solid State Ionics,* 287**,** 13–16.

SHARAFI, A., HASLAM, C. G., KERNS, R. D., WOLFENSTINE, J. & SAKAMOTO, J. 2017a. Controlling and correlating the effect of grain size with the mechanical and electrochemical properties of Li7La3Zr2O12solid-state electrolyte. *J. Mater. Chem. A,* 5**,** 21491–21504.

SHARAFI, A., KAZYAK, E., DAVIS, A. L., YU, S., THOMPSON, T., SIEGEL, D. J., DASGUPTA, N. P. & SAKAMOTO, J. 2017b. Surface Chemistry Mechanism of Ultra-Low Interfacial Resistance in the Solid-State Electrolyte Li7La3Zr2O12. *Chemistry of Materials,* 29**,** 7961–7968.

SHARAFI, A., MEYER, H. M., NANDA, J., WOLFENSTINE, J. & SAKAMOTO, J. 2016. Characterizing the Li–Li7La3Zr2O12 interface stability and kinetics as a function of temperature and current density. *Journal of Power Sources,* 302**,** 135–139.

SHI, C., ALEXANDER, G. V., O'NEILL, J., DUNCAN, K., GODBEY, G. & WACHSMAN, E. D. 2023a. All-Solid-State Garnet Type Sulfurized Polyacrylonitrile/Lithium-Metal Battery Enabled by an Inorganic Lithium Conductive Salt and a Bilayer Electrolyte Architecture. *ACS Energy Letters,* 8**,** 1803–1810.

SHI, C., HAMANN, T., TAKEUCHI, S., ALEXANDER, G. V., NOLAN, A. M., LIMPERT, M., FU, Z., O'NEILL, J., GODBEY, G., DURA, J. A. & WACHSMAN, E. D. 2023b. 3D

Asymmetric Bilayer Garnet-Hybridized High-Energy-Density Lithium-Sulfur Batteries. *ACS Appl Mater Interfaces,* 15**,** 751–760.

SINGH, D. K., HENSS, A., MOGWITZ, B., GAUTAM, A., HORN, J., KRAUSKOPF, T., BURKHARDT, S., SANN, J., RICHTER, F. H. & JANEK, J. 2022. Li6PS5Cl microstructure and influence on dendrite growth in solid-state batteries with lithium metal anode. *Cell Reports Physical Science,* 3.

SONG, S., PAKHARE, A., MEYERS, C., GAN, C., SHELDON, B., CARETTA, L., HIRTH, G., KIM, K.-S. & GUDURU, P. 2026. Stress-Controlled Dendrite Evolution in Solid Electrolytes. *Society of Engineering Science Annual Meeting 2026*.

SONG, S., SHI, C., PAKHARE, A., SHELDON, B. W. & GUDURU, P. R. 2025. Investigation of the Mechanical Properties of Porous Argyrodite Sulfide Electrolytes for All-Solid-State Batteries. *ACS Applied Energy Materials,* 8**,** 5636–5644.

THANGADURAI, V., KAACK, H. & WEPPNER, W. J. F. 2004. Novel Fast Lithium Ion Conduction in Garnet-Type Li5La3M2O12 (M = Nb, Ta). *Journal of the American Ceramic Society,* 86**,** 437**–**440.

TIAN, H.-K., LIU, Z., JI, Y., CHEN, L.-Q. & QI, Y. 2019. Interfacial Electronic Properties Dictate Li Dendrite Growth in Solid Electrolytes. *Chemistry of Materials,* 31**,** 7351–7359.

TRAN, M.-K., MEVAWALLA, A., AZIZ, A., PANCHAL, S., XIE, Y. & FOWLER, M. 2022. A Review of Lithium-Ion Battery Thermal Runaway Modeling and Diagnosis Approaches. *Processes,* 10.

WANG, S., ZHANG, Y., ZHANG, X., LIU, T., LIN, Y. H., SHEN, Y., LI, L. & NAN, C. W. 2018. High-Conductivity Argyrodite Li(6)PS(5)Cl Solid Electrolytes Prepared via Optimized Sintering Processes for All-Solid-State Lithium-Sulfur Batteries. *ACS Appl Mater Interfaces,* 10**,** 42279–42285.

WANG, Y., LI, S., WU, N., JIA, Q., HOKE, T., SHI, L., LI, Y. & CHEN, X. 2024. Thermal properties and lattice anharmonicity of Li-ion conducting garnet solid electrolyte Li6.5La3Zr1.5Ta0.5O12. *Journal of Materials Chemistry A,* 12**,** 18248–18257.

WANG, Z., MA, Q., WU, Z., ZHOU, J., ZHANG, Q., ZHANG, Q., LV, P., YU, K. & WEI, W. 2025. Thermal and ionic conductivity improvement of LAGP glass ceramic and fiber thermal drawing. *Ceramics International,* 51**,** 8615–8626.

WILSON, W. K. & YU, I. W. 1979. The use of the J-integral in thermal stress crack problems. *International Journal of Fracture,* 15**,** 377–387.

WOLFENSTINE, J., ALLEN, J. L., SAKAMOTO, J., SIEGEL, D. J. & CHOE, H. 2017. Mechanical behavior of Li-ion-conducting crystalline oxide-based solid electrolytes: a brief review. *Ionics,* 24**,** 1271–1276.

WOLFENSTINE, J., JO, H., CHO, Y.-H., DAVID, I. N., ASKELAND, P., CASE, E. D., KIM, H., CHOE, H. & SAKAMOTO, J. 2013. A preliminary investigation of fracture toughness of Li7La3Zr2O12 and its comparison to other solid Li-ionconductors. *Materials Letters,* 96**,** 117–120.

XIA, W., XU, B., DUAN, H., GUO, Y., KANG, H., LI, H. & LIU, H. 2016. Ionic Conductivity and Air Stability of Al-Doped Li(7)La(3)Zr(2)O(1)(2) Sintered in Alumina and Pt Crucibles. *ACS Appl Mater Interfaces,* 8**,** 5335–42.

XIE, W., DENG, Z., LIU, Z., FAMPRIKIS, T., BUTLER, K. T. & CANEPA, P. 2024. Effects of Grain Boundaries and Surfaces on Electronic and Mechanical Properties of Solid Electrolytes. *Advanced Energy Materials,* 14.

YAN, G., MALZBENDER, J., FU, S., GROSS, J. P., YU, S., EICHEL, R.-A. & SCHWAIGER, R. 2021. Fracture behavior of solid electrolyte LATP material based on micro-pillar splitting method. *Journal of the European Ceramic Society,* 41**,** 5240–5247.

YU, S., SCHMIDT, R. D., GARCIA-MENDEZ, R., HERBERT, E., DUDNEY, N. J., WOLFENSTINE, J. B., SAKAMOTO, J. & SIEGEL, D. J. 2015. Elastic Properties of the Solid Electrolyte Li7La3Zr2O12(LLZO). *Chemistry of Materials,* 28**,** 197–206.

YU, Z., GAN, C., SONG, S., GUDURU, P., KIM, K.-S. & SHELDON, B. W. 2026. Dendrite suppression in garnet electrolytes via thermally induced compressive stress. *Joule,* 10.

YUAN, J., ZHANG, Y., CHEN, F. & GU, Z. 2024. An overview of Joule heating in energy storage materials and applications. *Journal of Materials Chemistry C,* 12**,** 14729–14753.

ZHANG, B., YUAN, B., YAN, X., HAN, X., ZHANG, J., TAN, H., WANG, C., YAN, P., GAO, H. & LIU, Y. 2025. Atomic mechanism of lithium dendrite penetration in solid electrolytes. *Nat Commun,* 16**,** 1906.

ZHANG, C., YU, J., CUI, Y., LV, Y., ZHANG, Y., GAO, T., HE, Y., CHEN, X., LI, T., LIN, T., MI, Q., YU, Y. & LIU, W. 2024. An electron-blocking interface for garnet-based quasi-solid-state lithium-metal batteries to improve lifespan. *Nat Commun,* 15**,** 5325.

ZHANG, Y., MOTAHARI, S., WOODS, E. V., ZAEFFERER, S., SCHWEIZER, P., ZHANG, Z., LIU, Y., GAULT, B., ROTERS, F., RAABE, D., SCHEU, C., JOSHI, Y., ZHANG, S., LIU, C. & DEHM, G. 2026. Mechanically driven Li dendrite penetration in garnet solid electrolyte. *Nature,* 652**,** 912–918.

ZHOU, Y., LI, X., YANG, Y., HUANG, X. & TIAN, B. 2022. Production of Ta-Doped Li7La3Zr2O12 Solid Electrolyte with High Critical Current Density. *ACS Applied Energy Materials,* 5**,** 13817–13828.